Geophysical Journal International

Geophys. J. Int. (2026) **244**, 1–20
Advance Access publication 2026 January 14
Research Paper

https://doi.org/10.1093/gji/ggag018

Seismic tomography of Aluto volcano: insights into subsurface fluid distribution

Tesfahiwet Yemane, Petros Bogiatzis, John Michael Kendall and Jonathan Blundy

Department of Earth Sciences, University of Oxford, South Parks Road, Oxford, OX1 3AN, UK. E-mail: tesfahiwet.abraha@sjc.ox.ac.uk

Accepted 2026 January 9. Received 2026 January 6; in original form 2025 September 26

SUMMARY

Understanding subsurface fluid distribution in volcanic reservoirs is critical for geothermal energy development, critical mineral exploration and forecasting eruptions. Here, we use traveltime tomography to image the seismic velocity structure beneath Aluto volcano, the first pilot geothermal project in Ethiopia, located in the Main Ethiopian Rift. Using seismic data recorded from January 2012 to January 2014, we invert for the 3-D *P*-wave (V_p), *S*-wave (V_s) and V_p/V_s ratio. To reduce the non-uniqueness in interpretation, we also compare our results with previously published work on attenuation tomography and magnetotelluric images. Elevated V_p/V_s ratios [at 0 km below sea level (bsl)] around productive geothermal wells suggest high fluid content and/or elevated temperature. V_p/V_s values above 1.8 are observed along the caldera rims and hydrothermal vents, indicating fault and fracture systems as primary fluid conduits. High V_p/V_s below 6 km bsl likely reflects high-temperature areas or the presence of partial melt. In contrast, low V_p/V_s (< 1.5), low V_p, and average to high V_s beneath the caldera at around 5 km bsl is interpreted as a crystallized body with overpressurized gas volume formed during phase separation and transported upward through fractures and fault systems, accumulating at shallower levels. These findings highlight fluid pathways through the caldera rims and faults, with volatile-rich partial melt at greater depth beneath the caldera centre. Traveltime tomography thus offers a valuable constraints on subsurface fluid distribution and is valuable tool in geothermal exploration.

Key words: Magnetotellurics; Joint inversion; Body waves; Seismic attenuation; Seismic tomography; Volcano Seismology.

1 INTRODUCTION

Understanding the distribution of fluids in subsurface reservoirs within volcanic systems is important for geothermal energy development, critical mineral exploration that supports the energy transition toward net-zero emissions and for forecasting volcanic eruption (J. Blundy *et al.* 2021; B. Sanjuan *et al.* 2022; A.P. Jenkins *et al.* 2023; Gauntlett *et al.* 2023; T.S. Hudson *et al.* 2023; T. Yemane *et al.* 2025; Y. Liu *et al.* 2025). As the demand for renewable energy sources surges, the necessity for innovative approaches to energy generation and critical metal extraction becomes paramount. Geothermal fluids in volcanic systems can serve as a renewable energy source (T. Reinsch *et al.* 2017) and as a source of critical metals (Y.R. Smith *et al.* 2017; W.T. Stringfellow & P.F. Dobson 2021; J.M. Weinand et al 2023; L. Sajkowski *et al.* 2023; T. Yemane *et al.* 2025). To harness this potential, we focus on mapping the distribution of subsurface fluids using 3-D traveltime tomography at Aluto volcano, as a key challenge in geothermal drilling is finding exploitable fluid reservoirs (E. Jolie *et al.* 2021).

Aluto volcano, which is located in the Main Ethiopian Rift (MER), is home to Ethiopia's first pilot geothermal project, situated within the East African Rift System (EARS) (M.P. Hochstein *et al.* 2017). The EARS has significant energy potential for geothermal power generation (E. Jolie *et al.* 2019; N.E. Benti *et al.* 2023) and also holds potential for critical mineral reserves. Aluto is a restless silicic volcano (W. Hutchison *et al.* 2016b) that evolved with the development of the Wonji Fault Belt (WFB) (A. Agostini *et al.* 2011; W. Hutchison *et al.* 2015; G. Wadge *et al.* 2016; M. Wilks *et al.* 2020) with episodes of surface

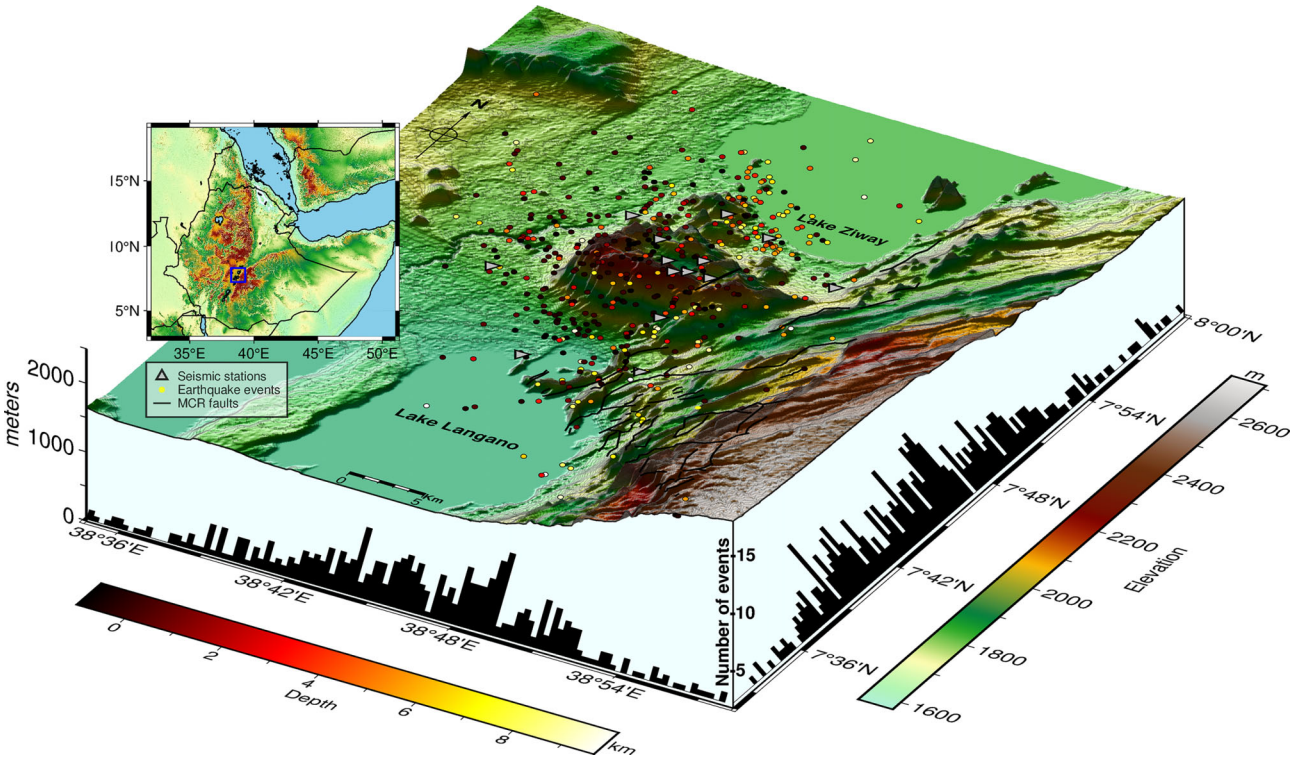

Figure 1. Seismicity at Aluto caldera from January 2012 to January 2014 used in the traveltime tomography. Events are colour-coded by depth, and seismic stations are indicated as grey triangles. Faults are indicated by solid black lines. The event distribution by longitude is displayed along the bottom axis, and the distribution by latitude is shown along the right axis. The majority of events at Aluto are shallow and are located at the centre of the caldera, and the seismic activity aligns parallel to the existing Artu Jawa Fault Zone (AJFZ).

deformation (J. Biggs *et al.* 2011; M. Wilks *et al.* 2017; Y. Birhanu *et al.* 2018). It is seismically active, with interconnected magmatic and hydrothermal systems (M. Wilks *et al.* 2020; T. Yemane *et al.* 2025). At the Aluto geothermal site, ten geothermal wells have been drilled, some of which are productive (LA-3, LA-6, LA-7, LA-8, LA-9, LA-10) and some are not (LA-1, LA-2 and LA-5) (M.P. Hochstein *et al.* 2017). Aluto is characterized by high-temperature areas with surface manifestations such as hydrothermal vents and CO_2 flux (J.A. Hunt *et al.* 2017). Detailed geological, geophysical and geochemical studies have been conducted to characterize the subsurface beneath Aluto volcano (B. Gizaw 1993; G. Gianelli & L.A. Teklemariam 1993; M. Teklemariam *et al.* 1996; D.G. Cornwell *et al.* 2006; K. Mickus *et al.* 2007; H. Saibi *et al.* 2012; F. Samrock *et al.* 2015; W. Hutchison *et al.* 2016a, b; M.L. Gleeson *et al.* 2017; A. Nowacki *et al.* 2018; B.A. Cherkose & H. Mizunaga 2018; J. Hübert *et al.* 2018; B.D. Mulugeta *et al.* 2021; F. Samrock *et al.* 2021; S. Regenspurg *et al.* 2022; F. Samrock *et al.* 2023; M.L.T. Dambly *et al.* 2023; W. Nigussie *et al.* 2023; T. Yemane *et al.* 2025). Recent absorption and scattering imaging of the volcano has delineated areas of high temperature and high fluid content, as well as structural features such as faults and fracture systems, which act as fluid pathways (T. Yemane *et al.* 2025).

Here, we use 3-D traveltime tomography to image the subsurface structure of Aluto volcano. Traveltime tomography has been used at global and local scales in volcanic systems (e.g. S. Hansen *et al.* 2004; I. Molina *et al.* 2005; C. Chiarabba & M. Moretti 2006; J. M. Lees 2007; I. Koulakov *et al.* 2013; E.I.M. Korger & V. Schlindwein 2014; G. Lin *et al.* 2014; T. Greenfield *et al.* 2016; M. Wilks *et al.* 2020; I. Koulakov *et al.* 2021; Gauntlett *et al.* 2023; E. A. Jiwani-Brown *et al.* 2024). Different rock properties, including lithology type, porosity, permeability, the presence of structural features such as faults, joints and fractures, and temperature affect seismic velocities (E. M. Syracuse *et al.* 2008; Gauntlett *et al.* 2023). Mapping the velocity structure, particularly the ratio of *P*-wave velocity to *S*-wave velocity (V_p/V_s) can therefore delineate areas of high fluid content, structural features, melt and supercritical brines (U. Muksin *et al.* 2013; M. Wilks *et al.* 2020). *S*-waves do not travel through fluids, and areas of high fluid content will have high V_p/V_s ratios. The V_p/V_s ratio has been used in different volcanic systems, where elevated values at shallower depths have been interpreted as melts (I. Koulakov *et al.* 2009; K. Jaxybulatov *et al.* 2011).

Traveltime tomography was previously conducted at Aluto by M. Wilks *et al.* (2020), however in this study, we use improved event locations determined using QuakeMigrate (T.S. Hudson *et al.* 2019; J.D. Smith *et al.* 2020; T. Yemane *et al.* 2025) and relocated with NonLinLoc (A. Lomax *et al.* 2000). We also adopt a different approach to perform the 3-D traveltime tomography by using finite-frequency kernels instead of ray paths (P. Bogiatzis *et al.* 2025). Ray theory is a high-frequency approximation that assumes the traveltime of a seismic wave is the line integral of slowness along the ray path between the source and receiver. In contrast, Fresnel volumes represent the traveltime as a weighted volume integral over the Earth's velocity structure (D. W. Vasco *et al.* 1995; J. Zhang *et al.* 2014). Moreover, the method enables efficient calculation of the full model resolution matrix, which is challenging in large inverse problems such as 3-D model

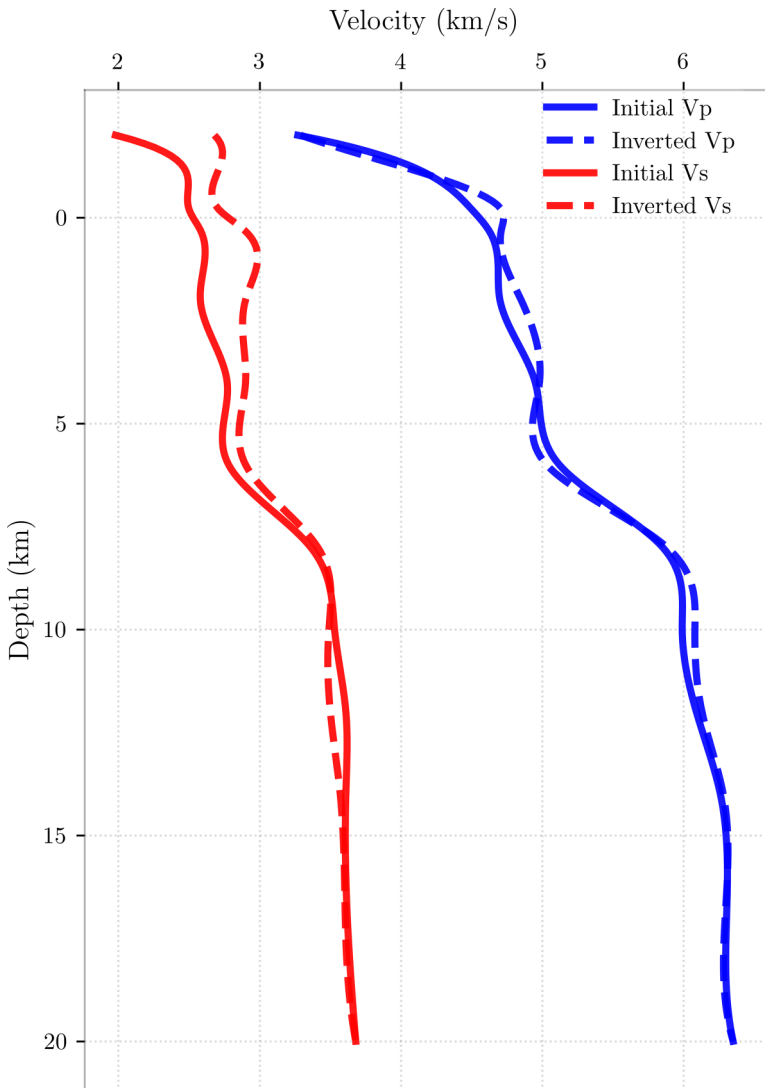

Figure 2. Initial 1-D velocity model used as the starting model for the 3-D traveltime tomography. The solid and dashed red lines represent the initial and inverted V_s, respectively, while the solid and dashed blue lines correspond to the initial and inverted V_p. The initial model is adapted from Wilks et al. (2017). We use the inverted V_p and V_s as the initial model for the 3-D traveltime tomography.

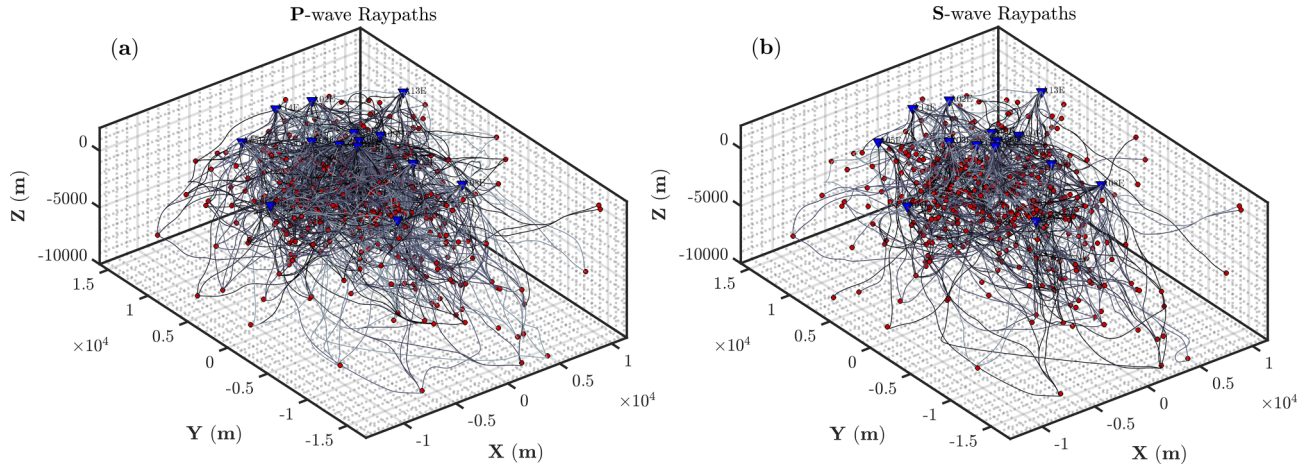

Figure 3. Ray path coverage for *P* waves (a) and *S* waves (b). Seismic stations are shown as blue inverted triangles, and earthquake hypocentres are marked by red circles. Ray paths, represented by black solid lines, connect the hypocentres to the stations.

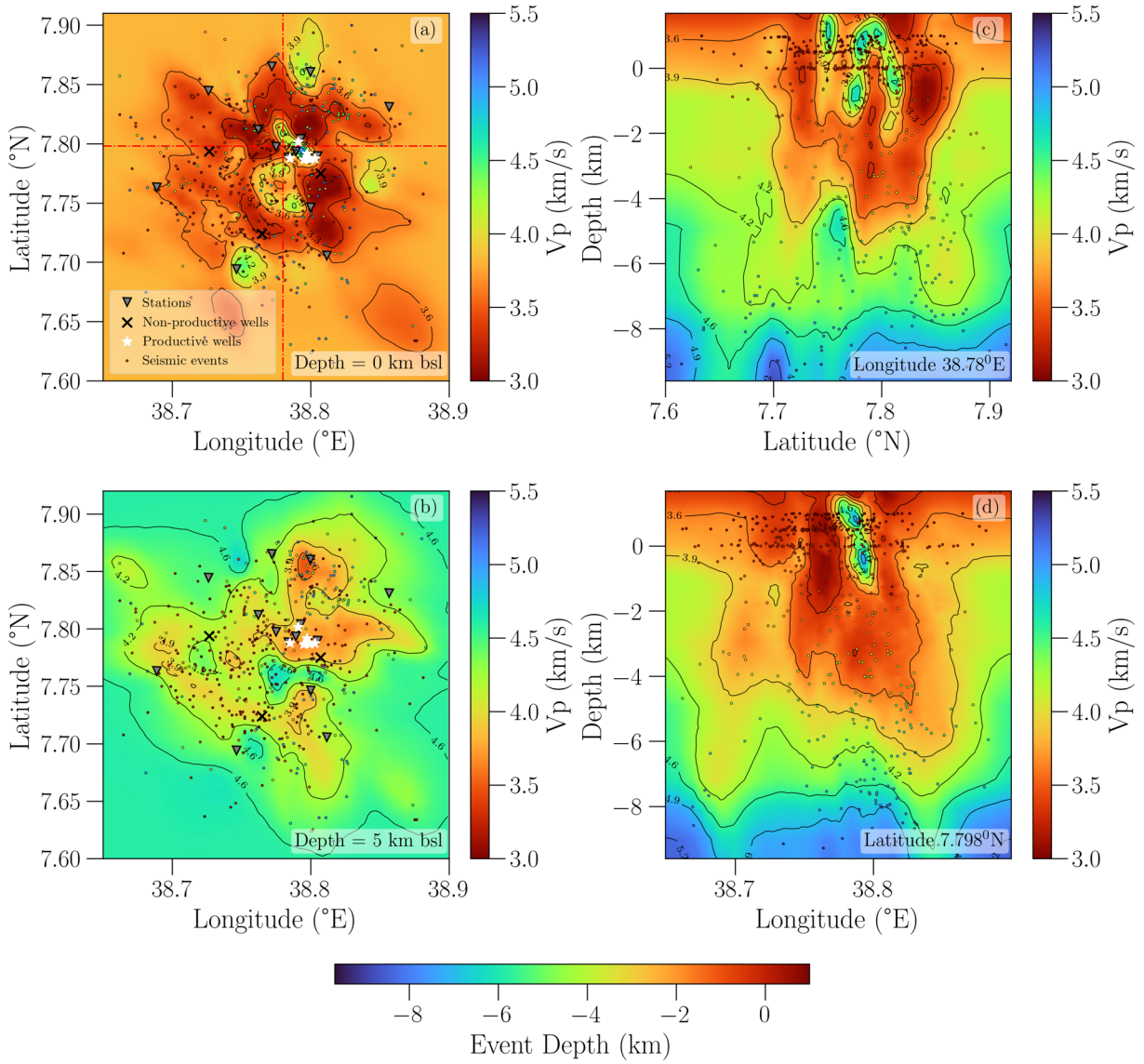

Figure 4. *P*-wave velocity model (V_p) from the final inversion iteration, shown at different depth slices [0 km (a) and 5 km (b) bsl] and along north–south (c) and east–west (d) cross-sections indicated by red dashed lines in (a). Seismic stations are shown as grey inverted triangles. Event locations are represented by small circles coloured by depth. Productive and non-productive geothermal wells are indicated by white stars and black crosses, respectively. The horizontal lineations of hypocentres at shallow depth in (c) and (d) reflect projection geometry and event selection, not depth-related imaging artefacts.

inversions. This calculation is important for evaluating the quality of the solution and the reliability of the imaged features. The 3-D joint inversion of *P* and *S* waves, along with the derived V_p/V_s ratio, enhances the ability to resolve key subsurface features. In particular, mapping the V_p/V_s distribution helps identify zones of elevated fluid content and structural pathways for fluid migration (U. Muksin *et al.* 2013). These high-resolution images provide deeper insights into the magmatic and hydrothermal systems beneath Aluto and can be used to assess the geothermal potential of the volcano and to explore next drilling targets. We also compare with previous studies, including attenuation and magnetotelluric imaging.

2 DATA AND METHODS

2.1 Earthquake catalogue

A network array of twelve Güralp CMG-6TD 30 s three-component broad-band seismometers, recording at a sampling rate of 100 Hz, was deployed at Aluto from January 2012 to January 2014 (The ARGOS Project 2012). We automatically detect and locate seismicity using QuakeMigrate (J. Drew *et al.* 2013; T.S. Hudson *et al.* 2019; J.D. Smith *et al.* 2020) and relocate using NonLinLoc (A. Lomax *et al.* 2000), a probabilistic location algorithm. We recorded 3401 events, and 2393 events (T. Yemane *et al.* 2025) after relocation, at and around Aluto volcano. For the local earthquake tomography, we selected events that fall within

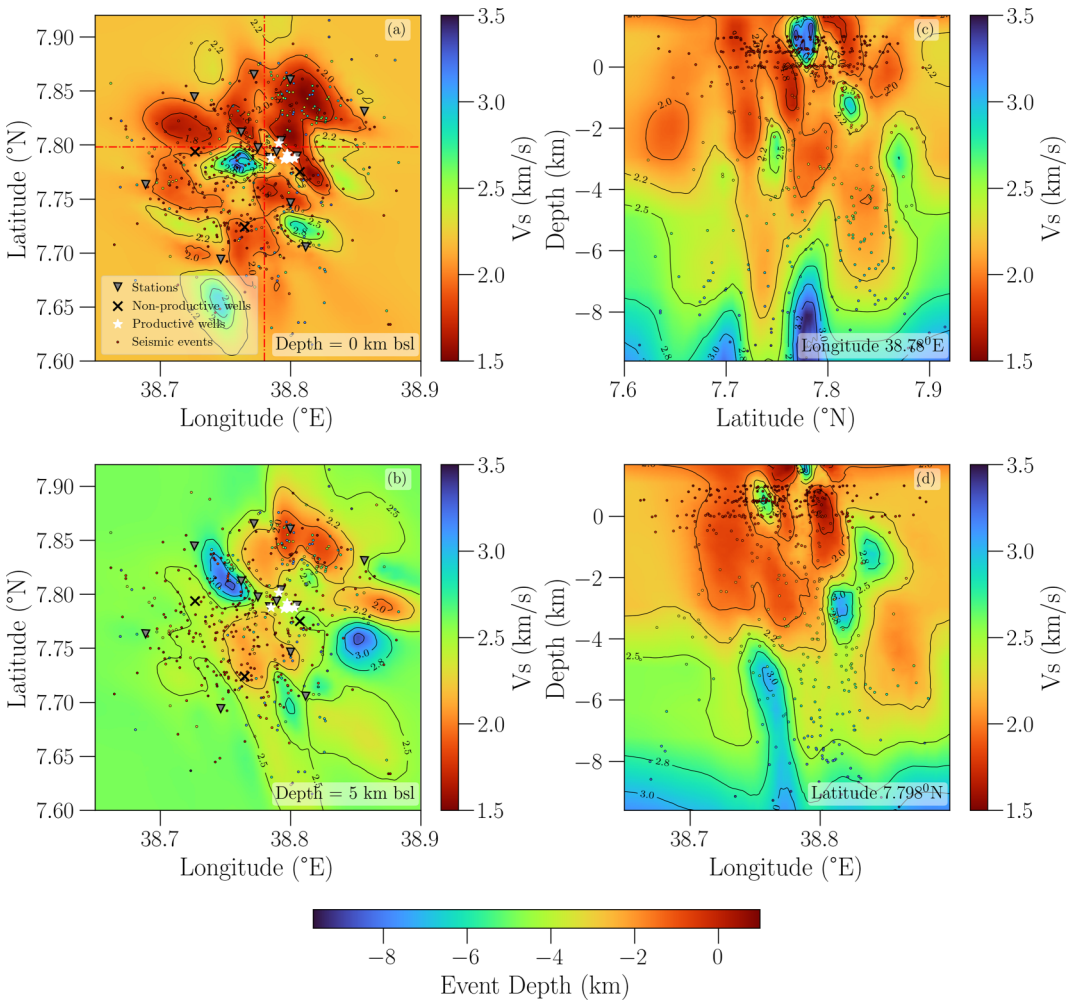

Figure 5. *S*-wave velocity model (V_s) for the last iteration, displayed at two depth slices [0 km (a) and 5 km (b) bsl], as well as along north–south (c) and east–west (d) cross-sections marked by red dashed lines (a). Grey inverted triangles indicate seismic stations, and earthquake hypocentres are shown as small circles colour-coded by depth. White stars represent productive geothermal wells, while black crosses indicate non-productive ones. The horizontal lineations of hypocentres at shallow depth in (c) and (d) reflect projection geometry and event selection, not depth-related imaging artefacts.

the network coverage, between depths of 1 km above sea level (asl) to 10 km below sea level (bsl). We further selected events with RMS less than 0.5 s, events which are recorded by at least three stations, and have both *P* and *S* waves recorded, to ensure good data quality. The number of events is reduced to 445, with 2176 *P*- and 1165 *S*-wave arrivals after the constraints, and this serves as the initial catalogue for updating the initial 1-D starting velocity model and for the 3-D local earthquake tomography. We updated the initial velocity model of M. Wilks *et al.* (2017) using the VELEST program (E. Kissling *et al.* 1994), which simultaneously determines the minimum 1-D velocity model (see Fig. 2).

2.2 Tomographic method

Local traveltime tomography is a commonly used method to investigate the velocity structure in volcanic systems (e.g. M. Wilks *et al.* 2020; Gauntlett *et al.* 2023). Models of V_p, V_s and V_p/V_s are produced by iteratively inverting *P* and *S* waves. Velocity models, particularly V_p/V_s ratio, can provide information about the subsurface structure, as it is influenced by lithology, fluid type, faults and fracture systems, all of which are important in geothermal systems. We use the tomographic inversion method of P. Bogiatzis *et al.* (2022b). The 3-D traveltime tomography algorithm jointly inverts *P*- and *S*-wave traveltime data and allows for the calculation of the model resolution matrix. The minimum 1-D velocity model obtained from the 1-D inversion is used as the initial velocity model for the 3-D simultaneous inversion.

We use the JIGSAW mesh generator (D. Engwirda 2015, 2016, 2018; D. Engwirda & D. Ivers 2016) to construct an irregular 3-D grid for the forward problem (P. Bogiatzis *et al.* 2022b). Grid node spacing ranges from 80 m in the central part of the volcano to 2200 m at the edges, incorporating fixed points for topography, seismic sources and receivers. Traveltime fields are computed using the shortest path method (I. Nakanishi & K. Yamaguchi 1986; P. Bogiatzis *et al.* 2021, 2025; E. W. Dijkstra 2022). The geometrical ray path is distributed within the first Fresnel volume to account for finite-frequency effects (Y. Liu *et al.* 2009; P. Bogiatzis *et al.* 2022a). The first Fresnel volume refers to the region surrounding a ray that has the greatest influence on the propagation of a band-limited wave (J. Spetzler & R. Snieder 2004). This involves the calculation of traveltime fields from sources to all grid points, as well as reciprocal fields from receivers (T. Watanabe *et al.* 1999). This reduces the limitations of ray-based forward solutions in traveltime tomography and is also less influenced by

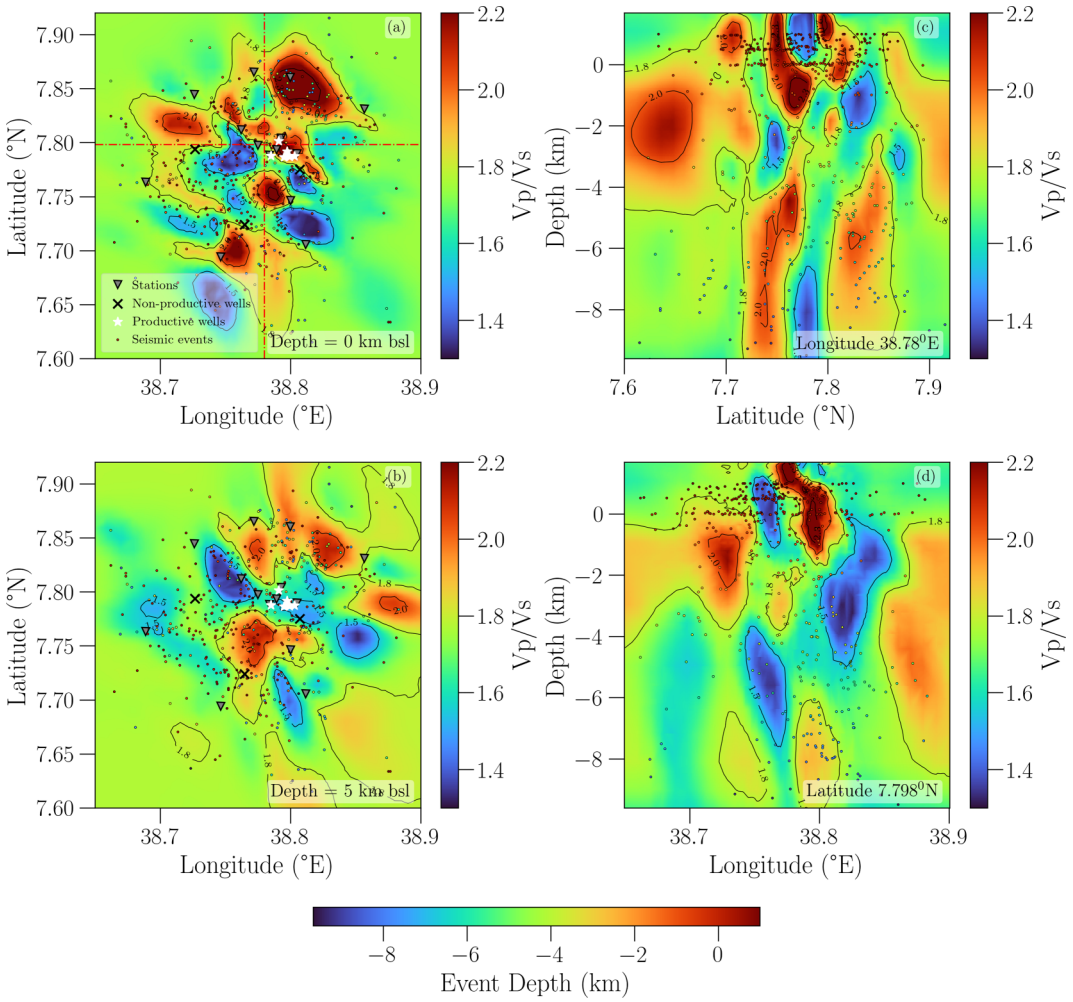

Figure 6. V_p/V_s model for the final iteration, shown at depth slices of 0 km (a) and 5 km (b) bsl, along with north–south (c) and east–west (d) cross-sections traced by red dashed lines (a). Seismic stations are marked by grey inverted triangles, and earthquake hypocentres are plotted as small circles colour-coded by depth. White stars denote productive geothermal wells, while black crosses indicate non-productive ones. The horizontal lineations of hypocentres at shallow depth in (c) and (d) reflect projection geometry and event selection, not depth-related imaging artefacts.

model parametrization compared to ray tomography (S. Husen & E. Kissling 2001).

We invert for *P*- and *S*-velocity structure and source locations simultaneously in the tomographic inversion. To obtain the V_p/V_s ratio, we divided the *P*-wave model by the *S*-wave model of the last iteration. During the inversion, a direct solver is used to invert the regularized normal equations of a least-squares problem. It solves for velocity perturbations and source corrections simultaneously using a least-squares method, where the updated velocity models are used to calculate new ray paths and traveltime residuals for the next iteration. This approach allows for the computation of the full model resolution matrix, which is important for assessing the solution reliability in nonlinear inversions. The solver utilizes sparse methods (T. A. Davis 2011) for computational efficiency. This helps to reduce the computational resources required for large 3-D tomographic inversions (P. Bogiatzis *et al.* 2016, 2019). We parametrized the initial velocity model by the 3-D grid of nodes, which are dense in the centre of the model and coarse on the edges, with air nodes above 2335 m elevation fixed at 343 m s^{-1} *P*-wave speed. To reduce the outliers, we use the generalized extreme studentized deviate test to weight the data (P. Bogiatzis *et al.* 2025).

Damping is used to stabilize the solution (E. Kissling *et al.* 2001) and reduce overfitting. Spatial smoothing is also used to ensure continuity across the model. To have physical consistency, cross-gradient constraints are used to ensure structural similarities between *P*- and *S*-velocity models (Gallardo and Meju 2004; Fregoso and Gallardo 2009; P. Bogiatzis *et al.* 2022b), while V_p/V_s ratio constraints enhance realistic velocity relationships based on prior geophysical knowledge. The optimal damping and smoothing constraints were chosen using the trade-off curve (D. Eberhart-Phillips 1986; R. C. Aster *et al.* 2018). After 40 iterations, with convergence tracked via residuals, refining velocity and source parameters progressively, we obtain an improvement of around 20 per cent, and the relocated source locations change by less than 20 m on average from the starting source locations.

2.3 Resolution analysis

The data coverage is assessed using the derivative weight sum (DWS) from the Jacobian matrix. DWS helps to quantify ray path density and sensitivity, offering a first-order estimate of data coverage (C. B. Biryol *et al.* 2013; M. Rezaeifar *et al.* 2016). However,

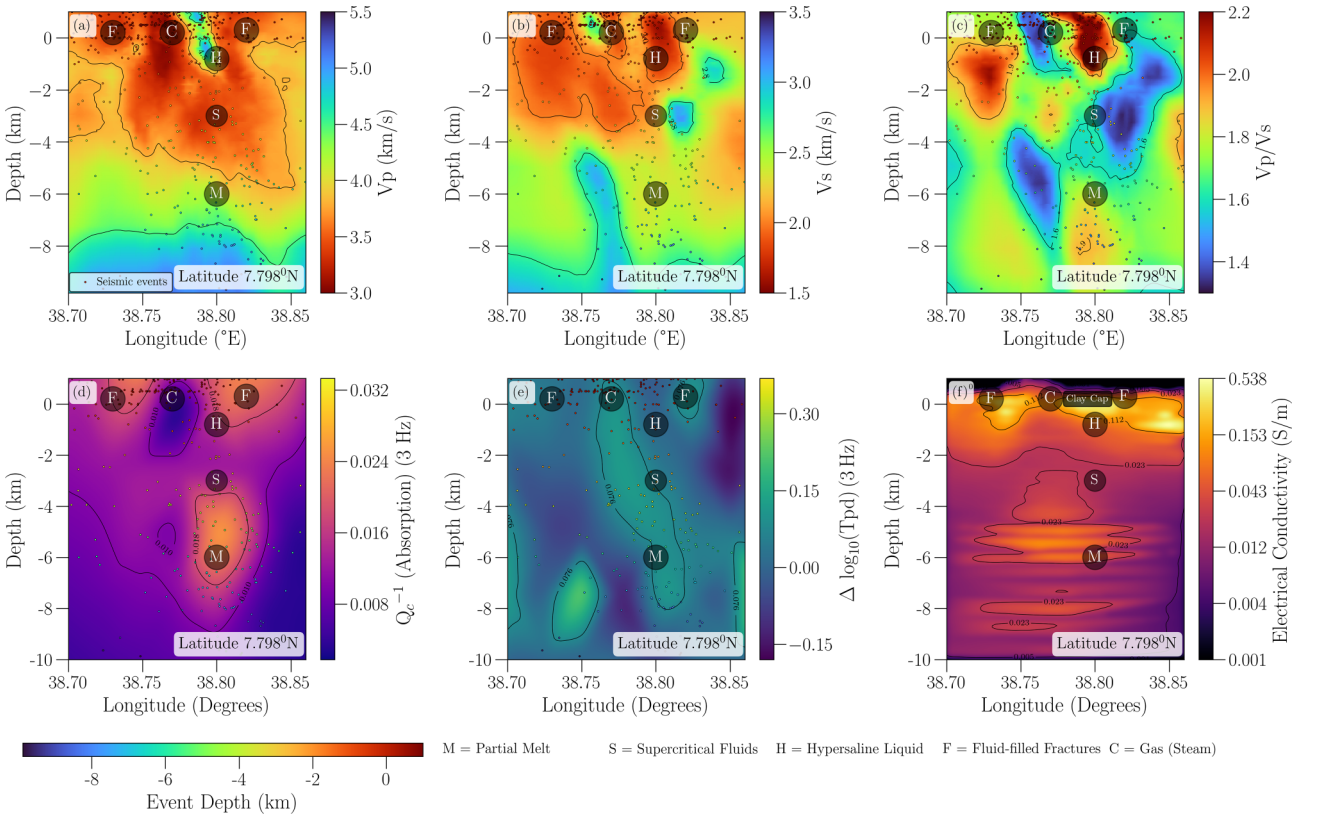

Figure 7. V_p, V_s and V_p/V_s models for the final iteration across longitude at a latitude of 7.798 °N, shown in panels (a), (b) and (c), respectively. Panels (d), (e) and (f) present absorption, scattering attenuation at 3 Hz (Yemane *et al.* 2025) and conductivity (Dambly *et al.* 2023) at the same latitude. Earthquake hypocentres are indicated by small circles, colour-coded by depth. Letters on the panels denote different regions beneath the Aluto volcanic system. The capital letters in each panel represent M (partial melt), S (supercritical fluids), H (hypersaline fluids), F (fracture-hosted fluids) and C (gas/steam).

it lacks details about the ray path linear dependencies, limiting its ability to show true resolution. To address this, the full model resolution matrix, computed directly via the solver, provides a detailed reliability evaluation. It shows how the velocity is well-constrained at each node, which also indicates the number of ray paths that pass through each node (C.H. Thurber 1981). We calculate the model resolution matrix for the last iteration. Diagonal elements show the degree of independent parameter resolution, with values close to one indicating a well-resolved region (W. Menke 2018). A node is considered well-resolved when its corresponding row in the resolution matrix has a peak on the diagonal, with minimal influence from off-diagonal elements.

The size and pattern of the off-diagonal elements show the smearing effect of each parameter within a volume encompassing the node (D. Eberhart-Phillips 1986; D. Eberhart-Phillips & A. J. Michael 1998). This helps to determine the smallest feature that can be resolved, referred to as the resolution length. We perform this analysis at different depth slices and in different regions of interest (see Figs 13, 14 and 15).

3 RESULTS

We located 2393 seismic events over the two-year period (T. Yemane *et al.* 2025) and selected 445 events for local earthquake tomography. The spatial distribution of the selected events is shown in Fig. 1, with hypocentral depths extending down to 10 km bsl. Majority of the events are clustered near the centre of the caldera, where most are shallow. Fig. 2 shows the updated initial 1-D velocity model used as the starting model for the 3-D inversion. The model uses M. Wilks *et al.* (2017) as the starting velocity model, which was originally developed by combining well-log data from the upper 2–3 km with a regional tomographic model (B. Gizaw 1993; G. Gianelli & L.A. Teklemariam 1993; E. Daly *et al.* 2008). There are slight differences between the initial and updated models. Fig. 3 illustrates the ray paths for both *P* and *S* waves. We observe dense ray coverage around the caldera, particularly for *P* waves. The station distribution and ray density ensure sufficient ray crossings, which improve the resolution of local subsurface features. This coverage contributes to a more accurate reconstruction of the velocity structure, thereby enhancing the characterization of the geothermal system.

Figs 4 and 5 show the V_p and V_s models obtained from the final iteration of the inversion, shown at two depth slices [0 and 5 km bsl, (a) and (b)] and along cross-sections extracted at selected latitude and longitude profiles (c and d). The cross-sections pass approximately through the centre of the caldera. At 0 km bsl [Figs 4 and 5(a)], we observe elevated V_p and V_s values at the caldera centre and around productive geothermal wells, whereas lower velocities are observed along the caldera rims. This pattern is more clearly resolved in the cross-sections [Figs 4 and 5, (c) and (d)], where both V_p and V_s are high directly beneath the caldera centre at shallow depths (≈ 0 km bsl). At 5 km bsl (Fig. 4b), V_p generally decreases, particularly beneath the caldera centre and geothermal wells, while V_s remains near background levels.

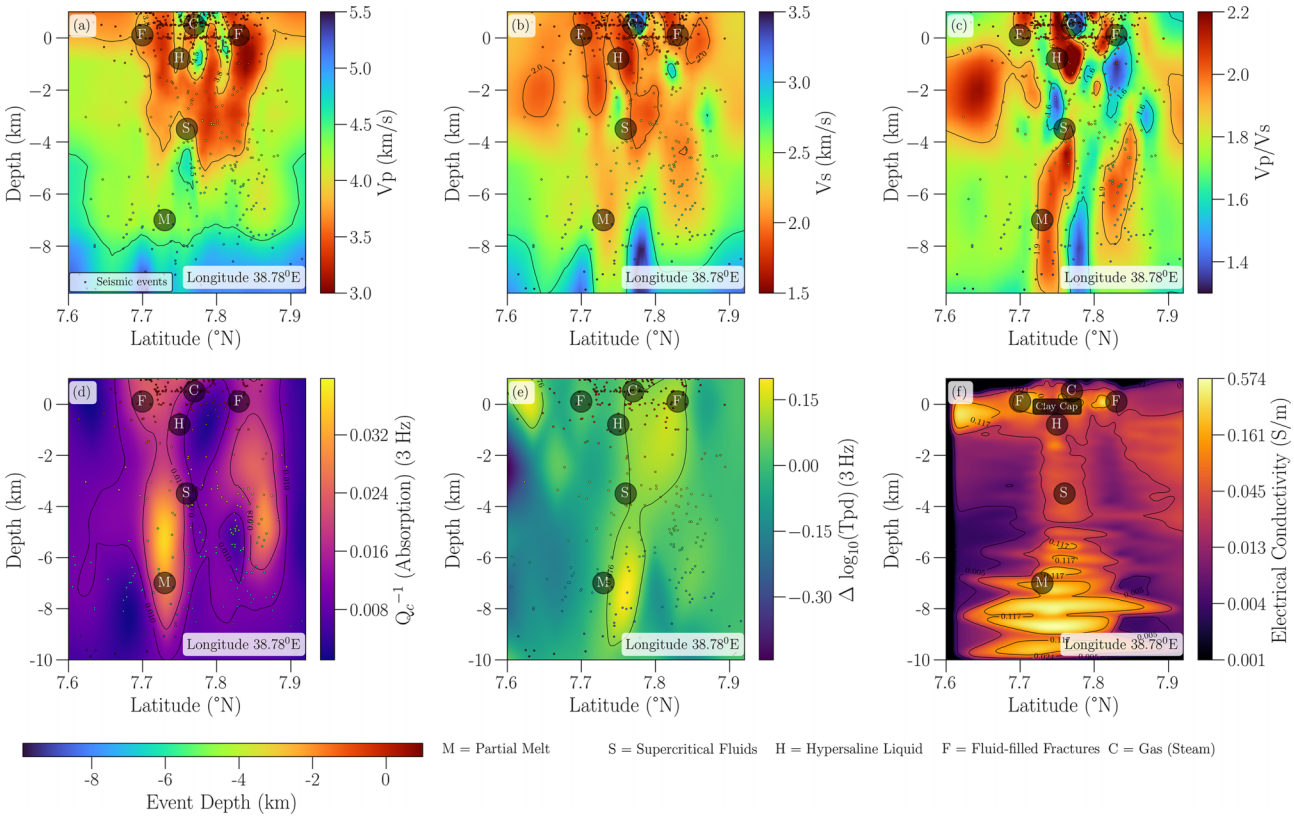

Figure 8. Panels (a), (b) and (c) display the final iteration for V_p, V_s and V_p/V_s models along latitude at 38.78^{0}E. Shown in panels (d), (e) and (f) are absorption, scattering attenuation at 3 Hz (Yemane *et al.*, 2025), and conductivity (Dambly *et al.* 2023) for the same longitude. Small circles mark earthquake hypocentres, with colours indicating depth. Different letters highlight distinct regions beneath the Aluto volcanic system. Capital letters in each panel indicate M (partial melt), S (supercritical fluids), H (hypersaline fluids), F (fracture-hosted fluids) and C (gas/steam).

This trend is also evident in the cross-sections, where V_p (Figs 4c and d) begins to decrease below $\approx$ 1 km bsl beneath the caldera centre, but remains relatively higher across the caldera rims. V_s (Figs 5c and d), in contrast, begins to decrease gradually between $\approx$ 1 km and 3 km bsl, but increases again below 4 km bsl, coinciding with areas of low V_p.

Fig. 6 presents the V_p/V_s model, derived by dividing the V_p and V_s velocity models, shown at two depth slices [0 and 5 km bsl (a) and (b)] and along the same cross-sections used for the V_p and V_s models. At 0 km bsl, high V_p/V_s values are observed around the central stations, extending to their north and south. In contrast, V_p/V_s beneath the central stations (caldera centre) decreases at 5 km bsl. The productive geothermal wells, indicated by white stars in Figs 6(a) and (b), are located at or slightly north of the central stations, and high V_p/V_s values are evident beneath these wells. Previous studies by T. Yemane *et al.* (2025) have reported high seismic attenuation and scattering beneath the productive geothermal wells. High conductivity is also observed near productive geothermal wells. Additionally, we observe low V_p/V_s anomaly beneath the centre of the caldera at around 5 km bsl, while elevated V_p/V_s values characterize the area below 6 km bsl and the caldera rims, where active hydrothermal vents are present.

There appear to be horizontal lineations of hypocentres at shallow depth in Figs 4, 5 and 6(c) and (d). These lineations are not associated with positive velocity gradients in either the initial or inverted 1-D velocity models. Because events are located independently prior to tomography, they do not reflect any depth control imposed by the 1-D model. Instead, the apparent horizontal structure results from event selection and projection geometry: events are restricted to a limited depth range and displayed in narrow cross-sections. The lineations are not systematic and do not persist in alternative cross-sections or in map/3-D views. Event quality control, together with iterative removal of poorly constrained events during inversion based on residuals, further ensures that the final velocity models are controlled by well-resolved hypocentres. Finally, resolution analyses confirm that the velocity features discussed lie within well-resolved regions and are not artefacts of event distribution or 1-D model dependence.

Figs 7 and 8 show cross-sections of V_p, V_s, V_p/V_s ratio, absorption attenuation, scattering attenuation and electrical conductivity along longitude at a latitude of 7.798 °N and along latitude at a longitude of 38.78 °E, respectively. The different methods consistently agree, identifying regions with similar physical properties. These regions are marked with capital letters for easier interpretation. They correspond to partial melt (M), supercritical fluids (S), hypersaline liquid or brine (H), fluid-filled fractures (F) and gas or steam in crystallized silicic volcanics (C). Table 1 summarizes their detailed characteristics. For example, the partial melt region (M) features relatively high V_p, intermediate V_s, elevated absorption, strong scattering, high conductivity and moderate seismicity. The conductivity cross-section particularly highlight the presence of partial melt. Areas with high scattering below the caldera centre show fluids migrating upward from this region toward shallower levels of the caldera, especially across

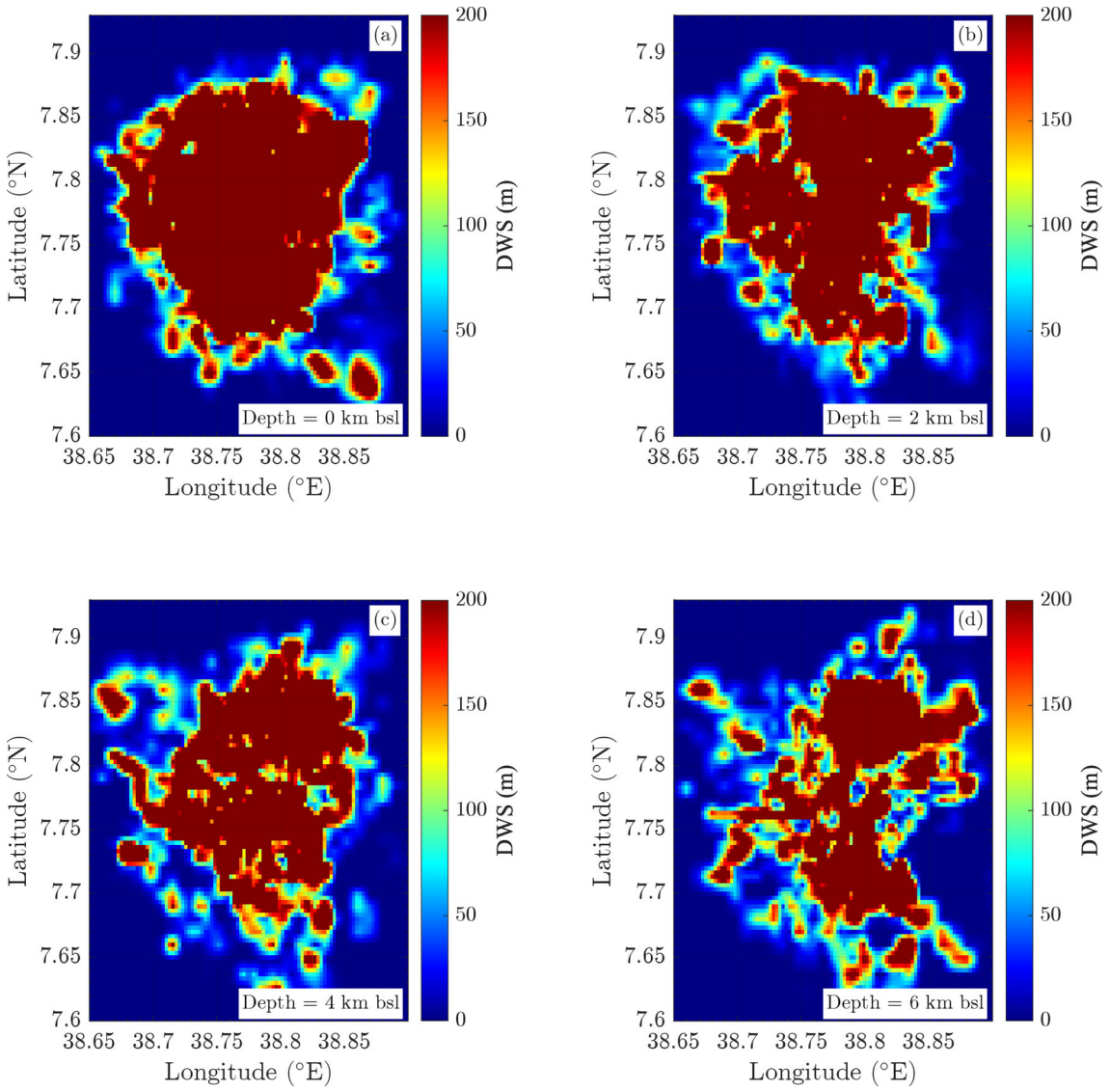

Figure 9. Derivative Weight Sum (DWS), representing the total ray path length and used to quantify ray path density for *P* waves, shown at different depth slices (0, 2, 4 and 6 km bsl). Deep red indicates regions of high ray density, while deep blue corresponds to areas of low ray density.

the Artu Jawa Fault Zone (AJFZ). This combination of seismic and magnetotelluric imaging (M.L.T. Dambly *et al.* 2023) provides a clear picture of melt and fluid distribution beneath the Aluto volcanic system.

Figs 9 and 10 display the data-weighted seismic ray coverage (DWS) for the final iteration of both *P* and *S* waves at different depth slices (0, 2, 4 and 6 km bsl). Overall, we observe good ray coverage across the depth slices, particularly for *P* waves, although sensitivity diminishes with increasing depth. The coverage for *S* waves is generally lower than that of *P* waves, especially below 6 km bsl. Regions of the model located farther from the station array are less well sampled, particularly at greater depths.

The full resolution matrix is computed at the final iteration, with the diagonal elements (RDE) shown in Figs 11 and 12 for the *P*- and *S*-wave models, respectively. To highlight regions of the model that can be independently resolved, we saturate the colour scale of the RDE due to the influence of strong damping. Although the RDE values are relatively low, primarily because of the applied damping and model parametrization, they still provide a reliable assessment of model resolution. Resolution is generally high in the central part of the caldera. Consistent with the DWS results, the *P*-wave model shows higher resolution than the *S*-wave model particularly at greater depth, mainly due to a greater number of *P*-wave rays.

To assess potential smearing effects, we examine the off-diagonal elements of the resolution matrix, which indicate how model parameters may be correlated or smeared. Figs 13 and 14 show horizontal sections of the off-diagonal elements at different depths. Fig. 13 illustrates smearing at the same node location across multiple depths, while Fig. 14 presents smearing at the same depth across different lateral positions. Similar smearing effects are observed in the vertical sections. Fig. 15 shows the vertical smearing effect at different depths. These patterns are also influenced by the applied damping and model parametrization. The similarity between the 0 and 6 km slices in Fig. 13 indicates that smearing is limited and behaves consistently at these depths, reflecting stable and well-resolved regions rather than a lack of depth sensitivity. Although the

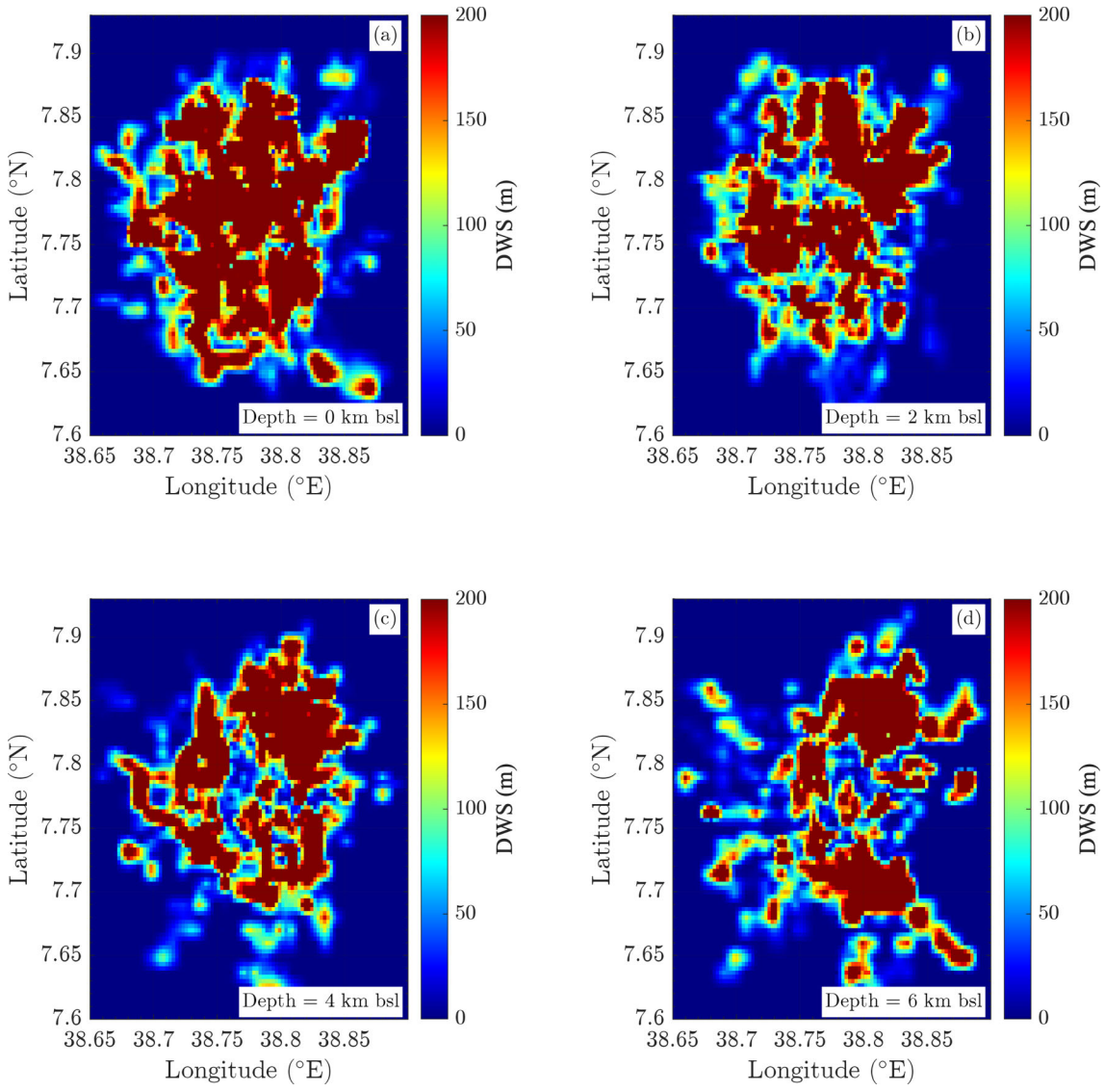

Figure 10. Derivative Weight Sum (DWS) for *S* waves, shown at different depth slices (0, 2, 4 and 6 km bsl), represent the total ray path length and quantify ray path density. Regions of high ray density are indicated by deep red, while areas with low ray density are shown in deep blue.

overall patterns may appear similar, they correspond to different model parameters and depths.

Fig. 16 shows a cross-section through the centre of the caldera. It combines the geophysical anomalies from Figs 7 and 8 with geological interpretation. The labelled areas match the features in Table 1, and the diagram highlights their arrangement and interactions. Specifically, the partial melt zone at depth serves as the main source of fluids and gases. The fluids move upward along structural pathways like the AJFZ. The shift from areas dominated by melt to zones rich in fluids shows how magmatic gases and fluids evolve and move toward the shallow hydrothermal system.

4 DISCUSSION

4.1 Solution quality

In traveltime tomography, the inversion process can introduce artefacts that do not reflect the true subsurface structure. To ensure the reliability of the velocity models, it is essential to evaluate the resolution quality. Model resolution is primarily influenced by ray path coverage, which can be assessed using various techniques (S. Husen *et al.* 2003), such as RDE. Both the RDE, which assesses solution quality, and the DWS values decrease with depth and beyond the bounds of the station array (Figs 11 and 12). This reduction is primarily due to limited ray coverage at greater depths and the sparse distribution of sources outside the network geometry. Ray coverage also decreases in regions with lower seismicity rates. Although the RDE values appear small (Figs 11 and 12), they still reflect a reliable solution, as their absolute magnitude is influenced by both damping and model parametrization. High damping suppresses model perturbations, and lowers RDE values (S. Husen *et al.* 2003). The examination of the off-diagonal elements of the resolution matrix does not reveal any significant smearing effect both horizontally and vertically (see Figs 13 and 14). Smearing effects are more significant in the vertical direction than in the horizontal.

We interpret the velocity models only in regions that are clearly well resolved, based on the derivative weight sum and the

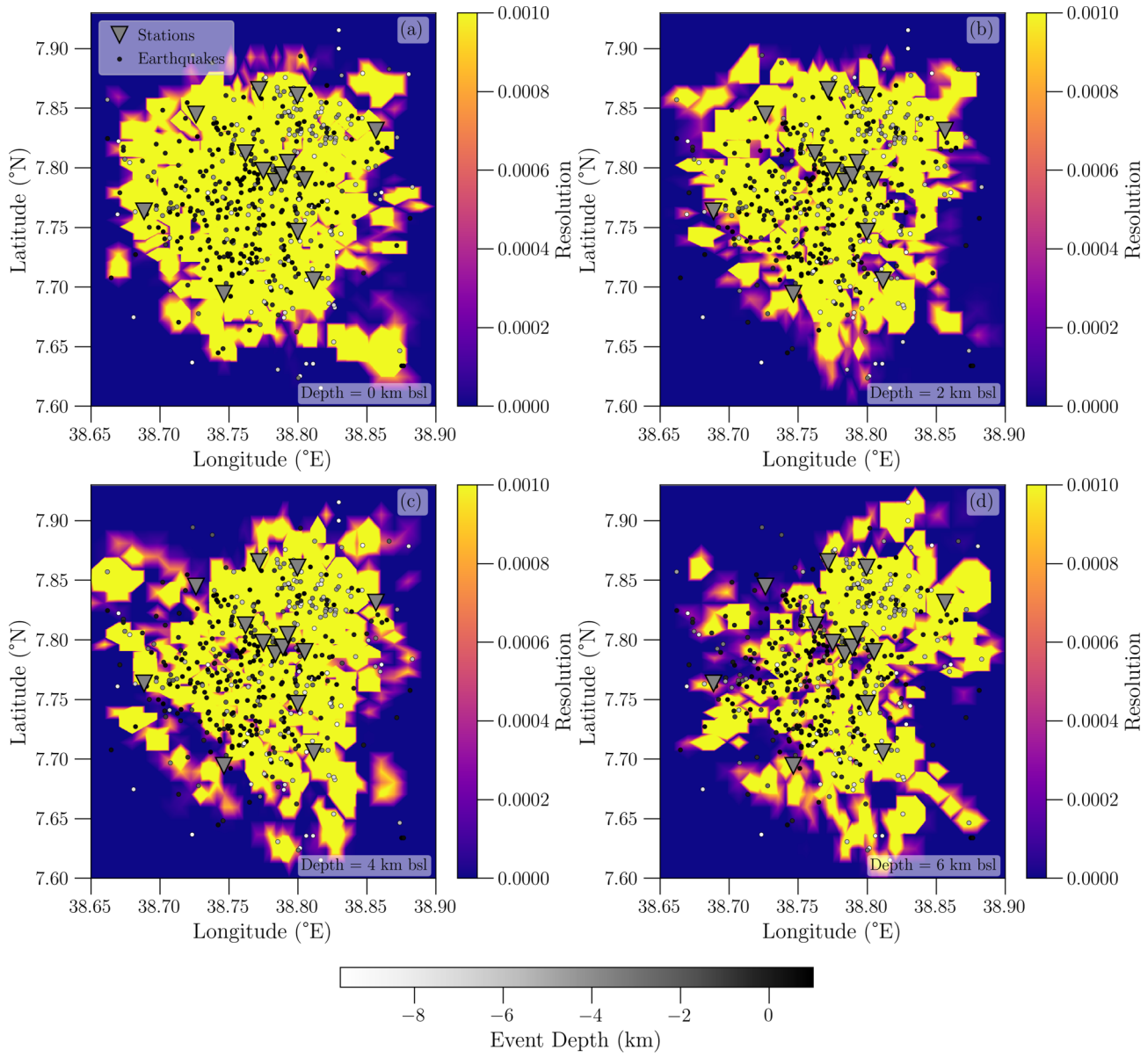

Figure 11. Diagonal elements of the resolution matrix (RDE) for *P* waves, shown at different depth slices (0, 2, 4 and 6 km bsl), calculated at the final inversion iteration. Seismic stations are indicated by grey inverted triangles, and event locations are shown as small circles coloured by depth. The resolution is shown exclusively by the colour scale of the diagonal elements of the resolution matrix, while the event depth colouring is included only to provide spatial context relative to the resolved regions. Deep yellow indicates areas of high resolution, while deep blue represents areas of low resolution. Overall, higher resolution is observed in regions with a greater density of earthquakes.

full model resolution matrix. The main velocity features shown in Figs 4, 5, 6 and the interpretation in 16 and summarized in Table 1 are located in areas of high ray coverage and good resolution, with limited smearing indicated by the off-diagonal elements. Instead of using extra synthetic recovery tests, we rely directly on the resolution information to guide our interpretation. These features are also supported by consistency with independent geophysical observations, including attenuation and magnetotelluric results.

4.2 Subsurface structure of the Aluto Caldera

Mapping the velocity structure beneath volcanoes helps to identify regions of high fluid content, partial melt and over pressurized gas which are important parameters for geothermal exploration, volcanic hazard assessment and understanding volcanic unrest (M. Wilks *et al.* 2020; Gauntlett *et al.* 2023). By combining V_p, V_s, V_p/V_s and other geophysical parameters, such as conductivity, absorption and scattering attenuation, and lithology, we identify distinct regions with unique geophysical signatures beneath the Aluto volcanic system. These regions are marked with capital letters in Figs 7 and 8. We describe and summarize the features of these regions in Table 1 and Fig. 16. A region of partial melt is interpreted at a depth of about 6 km (region M) from which supercritical fluids and gas migrate upward towards shallower levels of the caldera (S, H, F and C regions) through faults and fracture systems which act as pathways.

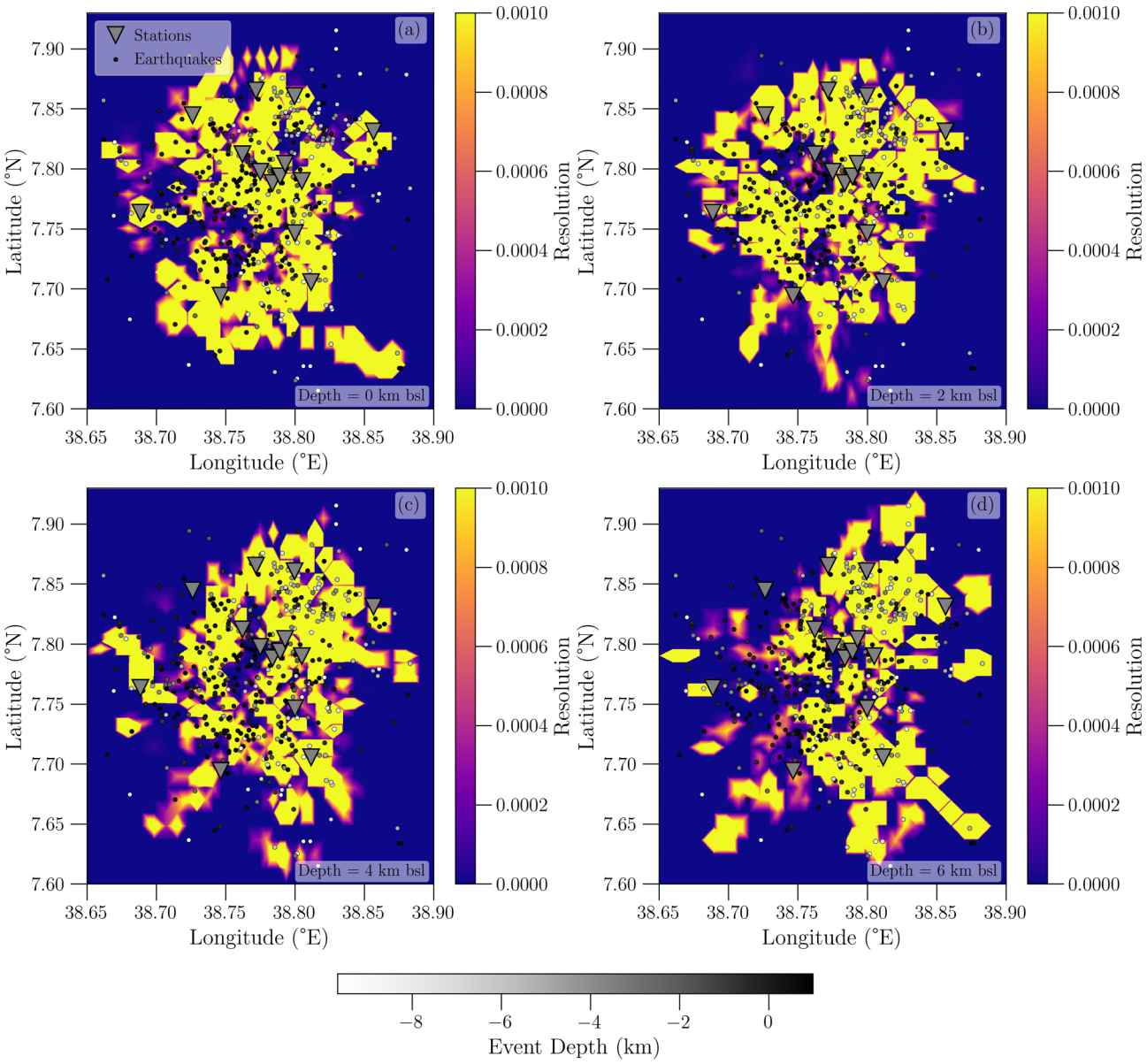

Figure 12. Resolution matrix diagonal elements (RDE) for *S* waves, calculated at the final inversion iteration and shown at depth slices of 0, 2, 4 and 6 km bsl. Grey inverted triangles mark seismic station locations, and small circles coloured by depth indicate earthquakes. The resolution is shown exclusively by the colour scale of the diagonal elements of the resolution matrix, while the event depth colouring is included only to provide spatial context relative to the resolved regions. High resolution regions are shown in deep yellow, while deep blue highlights areas of low resolution. Overall, higher resolution is observed in regions with a greater density of earthquakes.

At depths greater than 6 km bsl, high V_p/V_s anomalies are observed beneath the caldera, particularly along the caldera rims which we interpret as indicative of high temperatures and the possible presence of partial melt or melt pockets (region M) which is also characterized by high absorption, scattering and conductivity (Figs 7 and 8d, e and f). High V_p/V_s ratios are commonly associated with volcanic systems and are often attributed to zones of partial melt (G. Lin *et al.* 2014; T. Greenfield *et al.* 2016; M. Wilks *et al.* 2020; Gauntlett *et al.* 2023). This interpretation is supported by previous tomographic studies of volcanoes (e.g. L. De Siena *et al.* 2014; S. J. Ohlendorf *et al.* 2014). The effect of fluids on seismic velocities further supports this inference, while shear waves (*S*-waves) are strongly attenuated in the presence of fluids, particularly due to the zero shear modulus, *P* waves are affected primarily by fluid compressibility (T. Greenfield *et al.* 2016; M. Wilks *et al.* 2020; Gauntlett *et al.* 2023). In the presence of gas, *P*-wave velocities decrease, leading to lower V_p/V_s, whereas in the absence of gas, high V_p/V_s values may persist due to minimal *P*-wave attenuation (T. Vanorio *et al.* 2005). This distinction suggests that the high V_p/V_s, conductivity, absorption and scattering attenuation observed may correspond to high temperature, melt-rich zones. Moreover, between 6 and 10 km depth, the observed seismic velocity anomalies are unlikely to be controlled solely by fracture networks, which are less prevalent at these depths. Instead, the anomalies are more plausibly attributed to elevated temperatures or the presence of partial melt.

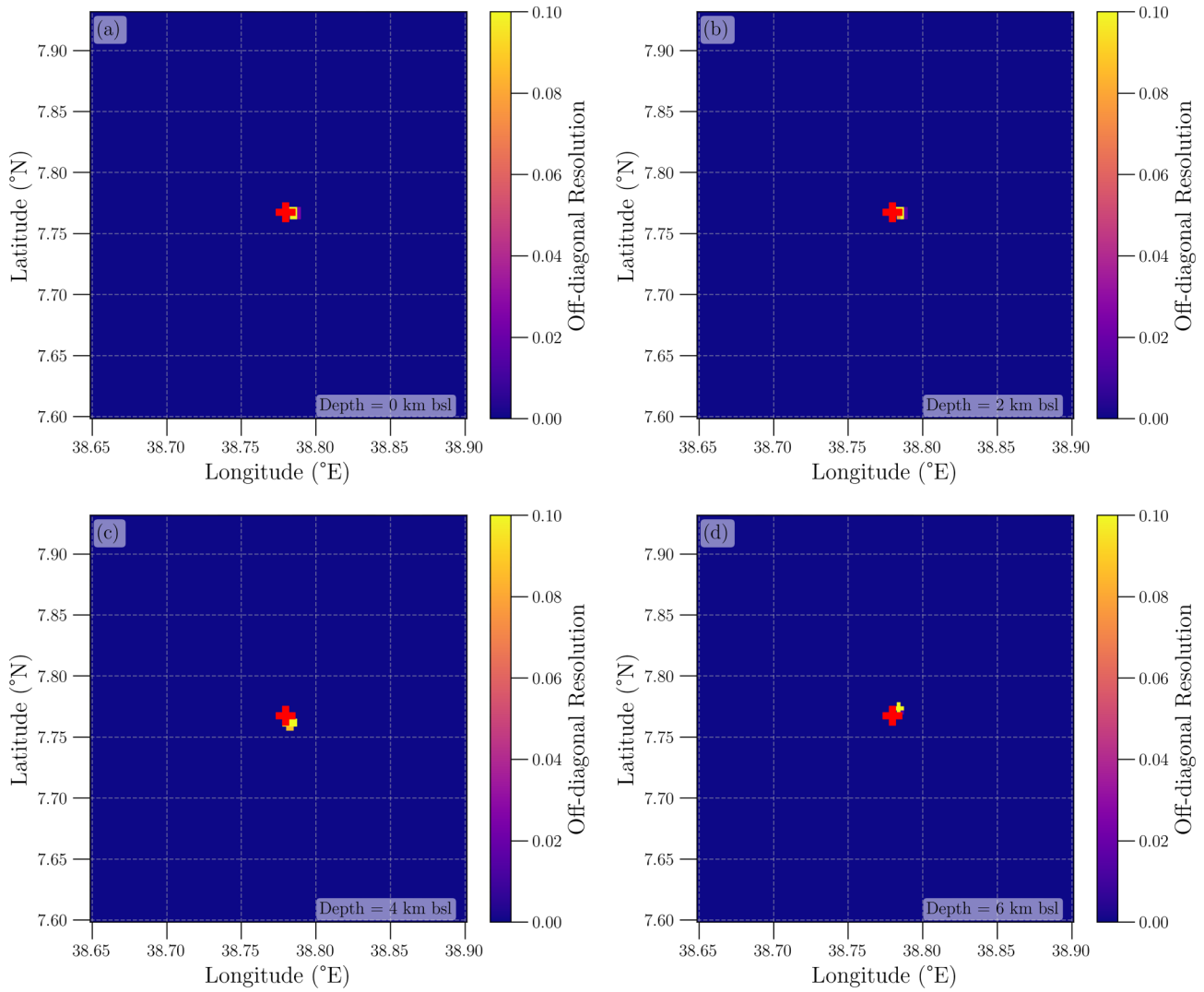

Figure 13. Off-diagonal elements of the resolution matrix (resolution length) at the final inversion iteration. Horizontal slices at different depths (0, 2, 4 and 6 km bsl) correspond to different model parameters. Red crosshair symbols indicate the locations of individual parameters. The similarity between the slices indicates limited smearing and stable, well-resolved structure, with similar patterns reflecting different parameters and depths rather than poor depth sensitivity.

Although earthquake activity decreases with depth, seismicity persists below the current imaging range (T. Yemane *et al.* 2025), indicating that the deeper crust does not have a large, laterally connected magma reservoir. Instead, it is more consistent with a high-temperature region containing localized melt pockets within a partially crystallized mush. Our analysis is restricted to the upper 10 km, where resolution is highest, but earthquakes extending below this depth (T. Yemane *et al.* 2025) demonstrate that the lower crust beneath Aluto is not entirely ductile. This interpretation is supported by previous geophysical studies including gravity, resistivity and magnetotelluric surveys, which show a dense, resistive body at shallow depth beneath the volcano, likely representing a solidified or partially solidified intrusive complex (K. Mickus *et al.* 2007; F. Samrock *et al.* 2015; B.A. Cherkose & H. Mizunaga 2018; J. Hübert *et al.* 2018; F. Samrock *et al.* 2021, 2023; M.L.T. Dambly *et al.* 2023). This interpretation is similar with earlier work by M. Wilks *et al.* (2017, 2020) who inferred a magmatic mush beneath Aluto, although they reported no deep seismicity.

Regions S and H, characterized by high conductivity, absorption and scattering, as well as medium to high V_p/V_s ratios, may represent supercritical and hypersaline fluids ascending from region M through fault and fracture systems that serve as pathways for fluids and/or gases. Region H is more conductive than Region S indicating the presence of brine solutions. Supercritical fluids can be compressed and behave like gases. Small pressure changes near their critical point lead to significant changes in density. This behaviour reduces the effective bulk modulus of saturated rocks. As a result, V_p decreases more than V_s (H. Ito *et al.* 1979). V_s mainly depends on the shear modulus of the rock, which remains unchanged since the fluid has zero shear strength. Consequently, V_p/V_s ratios drop below the normal range of region M (about 1.9 to 1.8), reaching around 1.7 or lower in region S, but remaining slightly higher in region H as brine concentrates when the fluid leaves its supercritical state. These ratios suggest the presence of supercritical fluids in volcanic or geothermal reservoirs.

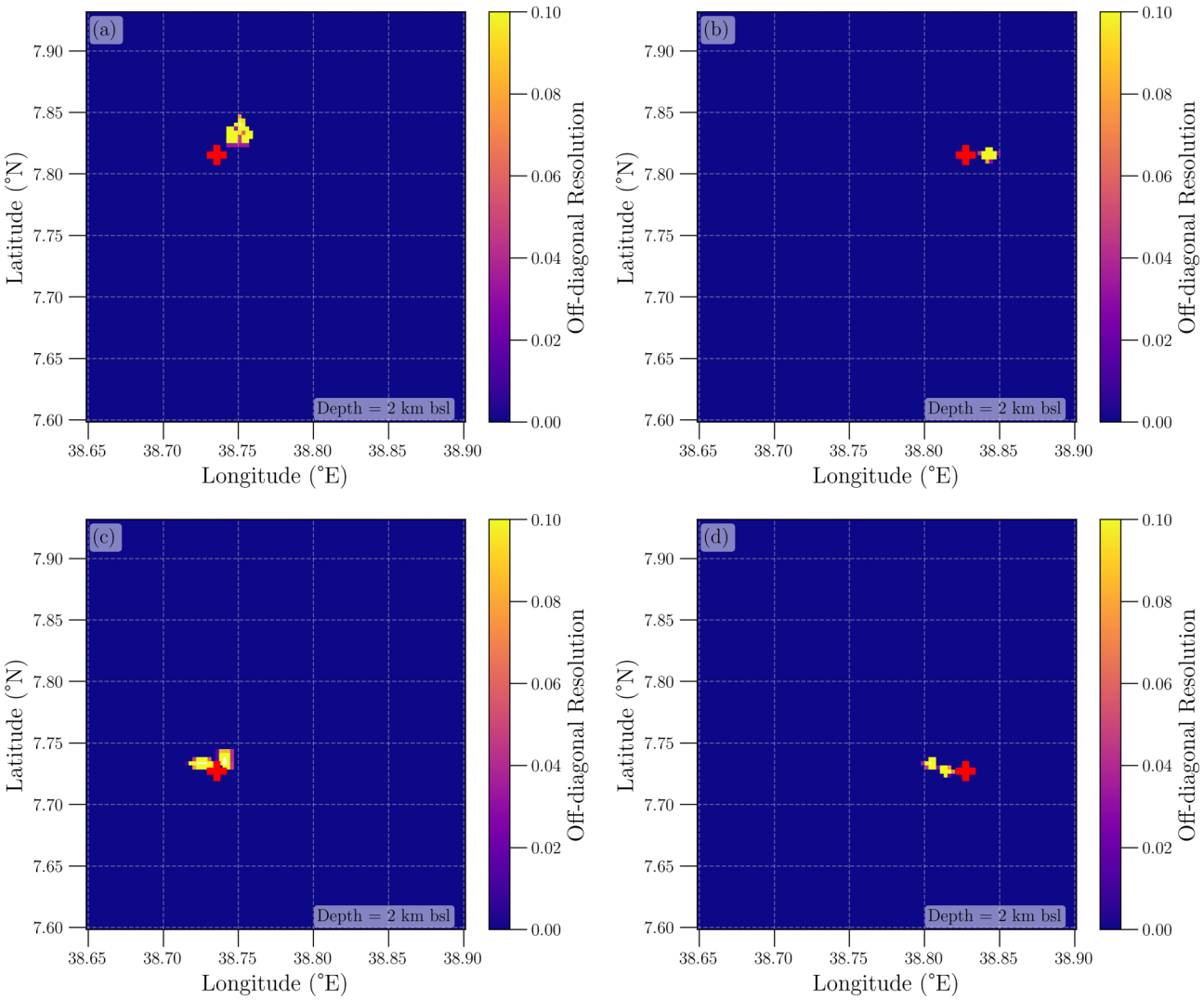

Figure 14. Off-diagonal elements of the resolution matrix (resolution length) at the final inversion iteration. Horizontal slices are shown at the same depth (2 km bsl) but correspond to different locations representing individual model parameters. Red crosshair symbols indicate the positions of these parameters.

A pronounced low V_p/V_s anomaly (1.5–1.7), unlabelled on the sides of region S, is observed beneath the centre of the caldera at around 5 km bsl in both the latitude and longitude sections (Figs 6c and d), characterized by low *P*-wave velocities (Fig. 4) and relatively high *S*-wave velocities (Fig. 5). We interpret this feature as overpressurized gas volume formed during phase separation from hypersaline fluid (brine) at the upper boundary of region S, although silica enrichment has an effect (Y. Zheng & T. Lay 2006). The gas is likely transported upward through fractures and fault systems, accumulating at shallower levels. The low V_p/V_s ratio ($<$1.5) observed at $\approx$ 5 km depth, particularly evident in Fig. 6 (d), is characterized with low conductivity, medium seismic absorption and scattering (Fig. 7, Figs 8d and e) (T. Yemane *et al.* 2025), which indicate the presence of gas content as gas bubbles are characterized by high absorption and scattering (T. Yemane *et al.* 2025).

In volcanic settings, elevated *P*-wave velocities are commonly associated with crystalline intrusive bodies (J. M. Lees 2007; Gauntlett *et al.* 2023), and gabbroic compositions that typically exhibit V_p/V_s ratios above 1.8. The significantly lower V_p/V_s in this region suggests a reduction in *P*-wave velocity due to the presence of pressurized gas, as previously demonstrated in experimental studies (M. N. Toksöz *et al.* 1976; N. I. Christensen 1996; L. Caricchi *et al.* 2008). *P*-wave velocities are higher in water-saturated rocks, while *S*-wave velocities are generally higher in dry or gas-saturated rocks (M. N. Toksöz *et al.* 1976).

The elevated *S*-wave velocities may reflect a rigid, solidified or crystallized magmatic intrusion, which supports efficient shear wave propagation (M. N. Toksöz *et al.* 1976). In contrast, the anomalously low *P*-wave velocities are consistent with a reduced bulk modulus caused by gas saturation, especially in regions undergoing fluid phase transitions (J. M. Lees & H. Wu 2000), for example, where liquid water transforms into steam in geothermal environments (H. Ito *et al.* 1979). This gas related *P*-wave reduction lowers the V_p/V_s ratio and serves as a diagnostic indicator of pressurized gas accumulation within the intrusive body (C. Chiarabba & M. Moretti 2006). Surface CO_2 emissions at Aluto exhibit a magmatic signature (J.A. Hunt *et al.* 2017), further supporting the presence of magmatic gas. Similar V_p/V_s anomalies linked to gas-bearing intrusions have been reported

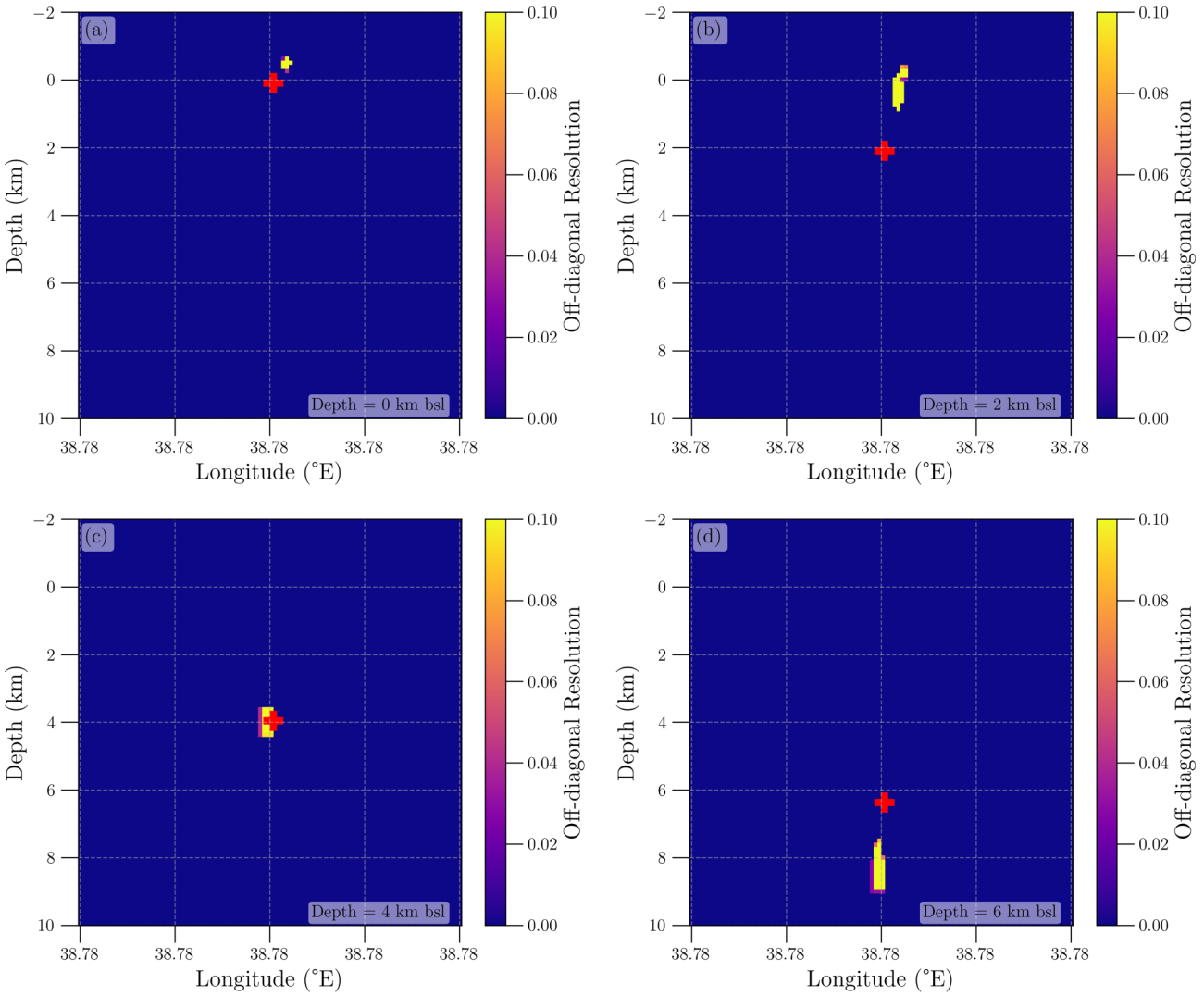

Figure 15. Vertical sections of the off-diagonal elements of the resolution matrix (resolution length) from the final inversion iteration, shown at depths of 0, 2, 4 and 6 km below sea level. Each slice corresponds to a different model parameter. Red crosshair symbols mark the locations of the evaluated parameters.

at other volcanic systems worldwide (e.g. C. Chiarabba & M. Moretti 2006; T. Greenfield *et al.* 2016; Gauntlett *et al.* 2023).

Regions of high V_p/V_s observed along the caldera rims (region F in Figs 7, 8 and 16), especially in the depth versus latitude and longitude sections (Figs 6c and d) are interpreted as zones of high fluid content (mainly liquid water) and/or temperature. These high V_p/V_s anomalies coincide with areas of high conductivity, seismic absorption and scattering (Figs 7 and 8d and e) (T. Yemane *et al.* 2025), where high absorption is typically associated with high fluid content and temperature, while enhanced scattering is attributed to heterogeneities or structural features such as faults or fracture systems. Moreover, hydrothermal and magmatic systems are likely interconnected through these fault and fracture networks, facilitating upward fluid and gas transport from regions of M to S, H, F and C in Figs 7 and 8. Additionally, high *b*-values (1.97) reported in Aluto volcano further support the presence of fluids, though elevated temperatures may also contribute (T. Yemane *et al.* 2025). We infer that faults that cross the caldera like the AJFZ and ring faults serve as primary fluid pathways, supported by observations of high scattering, CO_2 flux and hydrothermal activity along the caldera margins (J.A. Hunt *et al.* 2017) and high conductivity (see Figs 7 and 8f). The circulation of meteoric fluids in the upper few kilometres also increases the V_p/V_s ratio (I. Koulakov *et al.* 2020). The fluid source is likely a combination of meteoric and magmatic origins (region M), as previously reported, the CO_2 emissions have magmatic signature (W. Hutchison *et al.* 2016a) and the presence of exsolved fluids derived from magma (F. Samrock *et al.* 2021).

Fluid migration along these structures (faults and fracture systems) leads to partial rock saturation, consistent with the observations of the Aluto-Langano geothermal field as being water-dominated (B. Gizaw 1993; G. Gianelli & L.A. Teklemariam 1993; Genetu 2025) geothermal site. The fractured nature of the area promotes fluid permeability and saturation, as increased crack density, high pore fluid pressure and water-saturated rocks are known to elevate V_p/V_s ratios (X. Q. Wang *et al.* 2012).

The deepest geothermal wells at Aluto reach depths of approximately 0 km bsl. In the V_p/V_s depth slice at this level (Fig. 6a), high V_p/V_s [high V_p (Fig. 4) and moderate to low V_s (Fig. 5)] ratios are observed around the productive geothermal

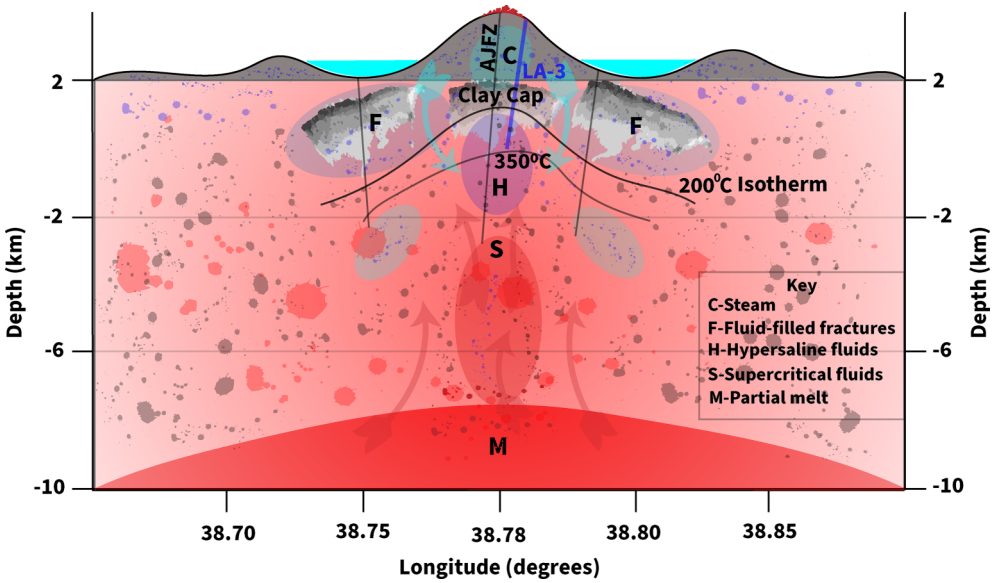

Figure 16. Schematic cross-section across longitude through the centre of the caldera. Distinct regions are denoted by capital letters: M = partial melt, S = supercritical fluids, H = hypersaline liquid (brine), F = fluid-filled fracture and C = gas within crystallized silicic volcanics. The corresponding geological and geophysical characteristics of these regions are summarized in Table 1. AJFZ refers to the Artu Jawa Fault Zone, and the blue line marks the productive geothermal well (LA-3), where the temperature at the well base approaches 350 °C.

Table 1. Geophysical interpretation of the different regions beneath the Aluto volcanic system.

Regions	V_p	V_s	V_p/V_s	Absorption	Scattering	Conductivity	Seismicity	Lithology	Interpretations
C	Low	High	Low	Medium	High	Medium	High	Silicic Volcanics	Gas in fractured volcanics
F	Low	Low	High	High	High	High	High	Silicic Volcanics	Fluid-filled fractured volcanics
H	High	Low	High	High	High	High	Medium	Tuffs and lavas, Bofa Basalt	Hypersaline fluids (Brines)
S	Medium	Medium	Medium	High	High	Medium	High	Bofa Basalt, Ignimbrite	Supercritial fluids
M	High	Medium	High	High	High	High	Medium	Ignimbrite	Partial melt

wells, marked by white stars, and are interpreted as indicative of high fluid content and elevated temperature. High conductivity is also observed near productive geothermal wells, aligning with the conceptual model of a high-enthalpy geothermal reservoir. Zoning takes on a mushroom-like geometry, with an upflow zone overlain by a conductive clay cap that generally develops at temperatures below 200 °C and becomes thinnest above the most productive wells (e.g. LA-3 and LA-6) (F. Samrock *et al.* 2015). In contrast, low V_p/V_s [high V_p (Fig. 4) and high to moderate V_s (Fig. 5)] ratios near non-productive wells which are indicated by white cross markers, likely reflect the absence of significant fluid saturation, consistent with earlier studies identifying these wells as impermeable (B. Gizaw 1993). Similar patterns have been reported in previous 3-D absorption and scattering imaging of the volcano (T. Yemane *et al.* 2025).

The shallow and narrow low V_p/V_s (high V_s but low V_p) anomaly near sea level beneath the caldera centre (region C in Figs 7 and 8) is interpreted as a gas reservoir that supplies CO_2 and other gas emissions at Aluto. Fluids exsolved from the partial melt (region M) likely evolve beyond the solvus and undergo phase separation into a hypersaline liquid (brine) and a vapour phase. Region S in Figs 7 and 8 is interpreted as a supercritical fluid zone that contains both brine and exsolved gases derived from region M. This region is characterized by high conductivity, scattering and absorption, consistent with the transport of fluids along a permeable conduit. Phase separation may occur near the upper boundary of region S, resulting in a brine-dominated zone (region H) and a shallow gas reservoir (region C).

Using the 3-D traveltime tomography and additional geophysical methods we are able to map the fluid distribution beneath the Aluto volcano. Geophysical signatures shows a zone with high V_p/V_s, elevated conductivity and strong scattering and absorption (region M). We interpret this as a partial melt body located at about 7 km bsl. This reservoir likely supplies fluids and volatiles to shallower areas, including the supercritical fluid zone (region S), the hypersaline brine zone (region H), the fluid-rich fracture network (region F) and the shallow gas reservoir (region C). Fluid and gas migration happens along fault and fracture systems that serve as permeable pathways, as shown by high scattering in the cross-sections. Similar features have been observed at other volcanic systems, such as Uturuncu (Y. Liu *et al.* 2025).

5 CONCLUSION

We present 3-D traveltime tomography images of Aluto volcano, the first pilot geothermal project located in, Ethiopia in the MER. We jointly invert *P*- and *S*-wave traveltime data and compute the full model resolution matrix to assess the quality of the solution. The DWS is used to evaluate data coverage, helping to quantify ray path density and sensitivity. We observe good coverage across different depth slices. The RDE, which provides a reliable measure of model resolution, also indicates high resolution, demonstrating the stability of the solution. Examination of the off-diagonal elements of the resolution matrix does not reveal any significant smearing effect.

Our results show elevated V_p/V_s ratios around productive geothermal wells at 0 km bsl, consistent with previous absorption and scattering studies (T. Yemane *et al.* 2025), which have been interpreted as indicative of high fluid content and/or elevated temperatures. V_p/V_s values exceeding 1.8 are observed around the caldera rims and hydrothermal vents, highlighting fault and fracture systems as primary conduits for fluid flow. In addition, high V_p/V_s ratios are detected below 6 km bsl, suggesting elevated temperatures or the possible presence of partial melt. Above this region we observe areas of supercritical fluids, brines and gas reservoir at shallow depth.

A low V_p/V_s ratio (<1.5) is observed beneath the caldera centre. This zone is also characterized by low *P*-wave velocity and relatively normal *S*-wave velocity. We interpret this feature as a crystallized body containing an overpressurized gas volume. The 3-D traveltime tomography results enable us to delineate regions of both high and low V_p/V_s ratios, providing an effective means to identify zones of elevated fluid content, high temperature and potential supercritical fluids. These findings are in good agreement with independent attenuation maps and offer valuable guidance for the future exploration of geothermal well targets.

ACKNOWLEDGMENTS

We thank SEIS-UK for providing seismic equipment under GEF loan 962 and for their technical assistance. We also acknowledge the contributions of the Ethiopian Electric Power Corporation (EEPCo) and the Geological Survey of Ethiopia (GSE) to the project. The seismic experiment and fieldwork were supported by the Bristol University Microseismic Projects (BUMPS). This work made use of the University of Oxford Advanced Research Computing (ARC) facility http://dx.doi.org/10.5281/zenodo.22558. We are thankful to Ian Bastow and the anonymous reviewers whose comments significantly improved the quality of the manuscript. TY is supported by a Clarendon Scholarship from the University of Oxford.

DATA AVAILABILITY

The XM seismic network and waveform data used in this study are openly available from the IRIS Data Service (The ARGOS Project 2012). Earthquakes were initially located using QuakeMigrate (C. Bacon *et al.* 2025) and relocated with NonLinLoc (A. Lomax *et al.* 2023). The 3-D seismic tomography was performed using Nstomo3D (P. Bogiatzis *et al.* 2022b), an open source software package. Seismic waveform processing was carried out using the ObsPy Python library (M. Beyreuther *et al.* 2010), and several figures were generated using the Generic Mapping Tools (GMT) suite (P. Wessel *et al.* 2019). All supporting data sets including the earthquake catalogue, borehole data (T. Yemane 2025), and V_p and V_s models from all iterations (T. Yemane 2026) are archived and publicly accessible via Zenodo (https://doi.org/10.5281/zenodo.18199403).

REFERENCES

Agostini, A., Bonini, M., Corti, G., Sani, F. & Mazzarini, F., 2011. Fault architecture in the Main Ethiopian Rift and comparison with experimental models: Implications for rift evolution and Nubia–Somalia kinematics, *Earth planet. Sci. Lett.,* **301**(3–4), 479–492.

Aster, R. C., Borchers, B. & Thurber, C. H., 2018. *Parameter Estimation and Inverse Problems,* Elsevier.

Bacon, C., Winder, T., Greenfield, T. & Bot, S., 2025. *QuakeMigrate v1.2.0 [Software],* Zenodo . doi:10.5281/zenodo.15185641.

Benti, N.E., Woldegiyorgis, T.A., Geffe, C.A., Gurmesa, G.S., Chaka, M.D. & Mekonnen, Y.S., 2023. Overview of geothermal resources utilization in Ethiopia: potentials, opportunities, and challenges, *Sci. Afr.,* **19,** e01562.

Beyreuther, M., Barsch, R., Krischer, L., Megies, T., Behr, Y. & Wassermann, J., 2010. ObsPy: A Python toolbox for seismology, *Seismol. Res. Lett.,* **81**(3), 530–533.

Biggs, J., Bastow, I.D., Keir, D. & Lewi, E., 2011. Pulses of deformation reveal frequently recurring shallow magmatic activity beneath the Main Ethiopian Rift, *Geochem. Geophys. Geosyst.,* **12**(9), doi:10.1029/2011GC003662.

Birhanu, Y., Wilks, M., Biggs, J., Kendall, J.M., Ayele, A. & Lewi, E., 2018. Seasonal patterns of seismicity and deformation at the Alutu geothermal reservoir, Ethiopia, induced by hydrological loading, *J. Volc. Geotherm. Res.,* **356,** 175–182.

Biryol, C. B., Leahy, G. M., Zandt, G. & Beck, S. L., 2013. Imaging the shallow crust with local and regional earthquake tomography, *J. geophys. Res. Solid Earth,* **118**(5), 2289–2306.

Blundy, J., Afanasyev, A., Tattitch, B., Sparks, S., Melnik, O., Utkin, I. & Rust, A., 2021. The economic potential of metalliferous sub-volcanic brines, *R. Soc. Open Sci.,* **8**(6), 202192.

Bogiatzis, P., Ishii, M. & Davis, T. A., 2016. Towards using direct methods in seismic tomography: computation of the full resolution matrix using high-performance computing and sparse QR factorization, *Geophys. J. Int.,* **205**(2), 830–836.

Bogiatzis, P., Ishii, M. & Davis, T. A., 2019. The Dulmage–Mendelsohn permutation in seismic tomography, *Geophys. J. Int.,* **218**(2), 1157–1173.

Bogiatzis, P., Rychert, C. A. & Harmon, N., 2021. Multiple graph realizations method: improving the accuracy and the efficiency of the shortest path method through random sampling, *Geophys. J. Int.,* **227**(1), 669–679.

Bogiatzis, P., Rychert, C. A., Harmon, N. & Xie, Y., 2022a. Fast calculation of spatial sensitivity kernels for scattered waves in arbitrary heterogeneous media using graph theory, *Geophys. J. Int.,* **230**(1), 654–672.

Bogiatzis, P., Vargemezis, G., Tsokas, G., Fikos, I., Amanatidou, E., Kordatos, N. & Polydoropoulos, K., 2022b. Nstomo3D: a new 3-D seismic tomography software and a case study from Apollonia, Greece, in *NSG2022 28th European Meeting of Environmental and Engineering Geophysics,* Vol. **2022(1),** pp. 1–5, European Association of Geoscientists and Engineers.

Bogiatzis, P., Vargemezis, G., Tsokas, G., Amanatidou, E., Karamitrou, A. & Karaoulis, M., 2025. Revealing the internal structure of the great tumulus of Apollonia by means of seismic tomography, *Archaeol. Prospect.,* **32**(1), 235–246.

Caricchi, L., Burlini, L. & Ulmer, P., 2008. Propagation of *P* and *S*-waves in magmas with different crystal contents: insights into the crystallinity of magmatic reservoirs, *J. Volc. Geotherm. Res.,* **178**(4), 740–750.

Cherkose, B.A. & Mizunaga, H., 2018. Resistivity imaging of Aluto-Langano geothermal field using 3-D magnetotelluric inversion, *J. Afr. Earth Sci.,* **139,** 307–318.

Chiarabba, C. & Moretti, M., 2006. An insight into the unrest phenomena at the Campi Flegrei caldera from V_p and V_p/V_s tomography, *Terra Nova,* **18**(6), 373–379.

Christensen, N. I., 1996. Poisson's ratio and crustal seismology, *J. geophys. Res.: Solid Earth,* **101**(B2), 3139–3156.

Cornwell, D.G., Mackenzie, G.D., England, R.W., Maguire, P.K.H., Asfaw, L.M. & Oluma, B., 2006. Northern Main Ethiopian Rift crustal structure from new high-precision gravity data, *Geol. Soc. London, Special Publ.,* **259**(1), doi: 10.1144/GSL.SP.2006.259.01.23.

Daly, E., Keir, D., Ebinger, C. J., Stuart, G. W., Bastow, I. D. & Ayele, A., 2008. Crustal tomographic imaging of a transitional continental rift: The Ethiopian rift, *Geophys. J. Int.,* **172**(3), 1033–1048.

Dambly, M.L.T., Samrock, F., Grayver, A.V. & Saar, M.O., 2023. Insights on the interplay of rifting, transcrustal magmatism and formation of geothermal resources in the central segment of the Ethiopian Rift revealed by 3-D magnetotelluric imaging, *J. geophys. Res.: Solid Earth,* **128**(7), e2022JB025849.

[dataset, T., 2026. *Vp and Vs models of Aluto Volcano in the Main Ethiopian Rift (MER),* Zenodo, doi:10.5281/zenodo.18199403.

Davis, T. A., 2011. Algorithm 915, SuiteSparseQR: Multifrontal multithreaded rank-revealing sparse QR factorization, *ACM Trans. Math. Softw.,* **38**(1), 1–22.

De Siena, L., Thomas, C., Waite, G. P., Moran, S. C. & Klemme, S., 2014. Attenuation and scattering tomography of the deep plumbing system of Mount St. Helens, *J. geophys. Res.: Solid Earth,* **119**(11), 8223–8238.

Dijkstra, E. W., 2022. A note on two problems in connexion with graphs, in *Edsger Wybe Dijkstra: His Life, Work, and Legacy,* pp. 287–290, eds Apt, K.R. & Hoare, T., Association for Computing Machinery.

Drew, J., White, R.S., Tilmann, F. & Tarasewicz, J., 2013. Coalescence microseismic mapping, *J. geophys. Int.,* **195**(3), 1773–1785.

Eberhart-Phillips, D., 1986. Three-dimensional velocity structure in northern California Coast Ranges from inversion of local earthquake arrival times, *Bull. seism. Soc. Am.,* **76**(4), 1025–1052.

Eberhart-Phillips, D. & Michael, A. J., 1998. Seismotectonics of the Loma Prieta, California, region determined from three-dimensional V_p, V_p/V_s, and seismicity, *J. geophys. Res.: Solid Earth,* **103**(B9), 21 099–21 120.

Engwirda, D., 2015. Voronoi-based point-placement for three-dimensional Delaunay-refinement, *Proc. Eng.,* **124,** 330–342.

Engwirda, D., 2016. Conforming restricted Delaunay mesh generation for piecewise smooth complexes, *Proc. Eng.,* **163,** 84–96.

Engwirda, D. & Ivers, D., 2016. Off-centre Steiner points for Delaunay-refinement on curved surfaces, *Computer-Aided Design,* **72,** 157–171.

Engwirda, D., 2018. Generalised primal-dual grids for unstructured co-volume schemes, *J. Comput. Phys.,* **375,** 155–176.

Fregoso, E. & Gallardo, L.A., 2009. Cross-gradients joint 3D inversion with applications to gravity and magnetic data, *Geophysics,* **74**(4), L31–L42.

Gallardo, L.A. & Meju, M.A., 2004. Joint two-dimensional DC resistivity and seismic travel time inversion with cross-gradients constraints, *J. geophys. Res.: Solid Earth,* **109**(B3), doi:10.1029/2003JB002610.

Gauntlett, M. *et al.*, 2023. Seismic tomography of Nabro Caldera, Eritrea: insights into the magmatic and hydrothermal systems of a recently erupted volcano, *J. geophys. Res.: Solid Earth,* **128**(5), e2022JB025742.

Genetu, M., 2025. Assessment of geothermal energy in Aluto-Langano and Tulu-Moye, Central Ethiopia, *Geol. J.,* **60**(1), 64–72.

Gianelli, G. & Teklemariam, M., 1993. Water-rock interaction processes in the Aluto-Langano geothermal field (Ethiopia), *J. Volc. Geotherm. Res.,* **56**(4), 429–445.

Gizaw, B., 1993. Aluto-Langano geothermal field, Ethiopian Rift Valley: physical characteristics and the effects of gas on well performance, *Geothermics,* **22**(2), 101–116.

Gleeson, M.L., Stock, M.J., Pyle, D.M., Mather, T.A., Hutchison, W., Yirgu, G. & Wade, J., 2017. Constraining magma storage conditions at a restless volcano in the Main Ethiopian Rift using phase equilibria models, *J. Volc. Geotherm. Res.,* **337,** 44–61.

Greenfield, T., White, R.S. & Roecker, S., 2016. The magmatic plumbing system of the Askja central volcano, Iceland, as imaged by seismic tomography, *J. geophys. Res.: Solid Earth,* **121**(10), 7211–7229.

Hansen, S., Thurber, C., Mandernach, M., Haslinger, F. & Doran, C., 2004. Seismic velocity and attenuation structure of the east rift zone and south flank of Kilauea Volcano, Hawaii, *Bull. seism. Soc. Am.,* **94**(4), 1430–1440.

Hochstein, M.P., Oluma, B. & Hole, H., 2017. Early exploration of the Aluto geothermal field, Ethiopia (History of discovery well LA-3), *Geothermics,* **66,** 73–84.

Hübert, J., Whaler, K. & Fisseha, S., 2018. The electrical structure of the central Main Ethiopian Rift as imaged by magnetotellurics: implications for magma storage and pathways, *J. geophys. Res.: Solid Earth,* **123**(7), 6019–6032.

Hudson, T.S., Smith, J., Brisbourne, A.M. & White, R.S., 2019. Automated detection of basal icequakes and discrimination from surface crevassing, *Ann. Glaciol.,* **60**(79), 167–181.

Hudson, T.S., Kendall, J.-M., Blundy, J.D., Pritchard, M.E., MacQueen, P., Wei, S.S., Gottsmann, J.H. & Lapins, S., 2023. Hydrothermal fluids and where to find them: using seismic attenuation and anisotropy to map fluids beneath Uturuncu volcano, Bolivia, *Geophys. Res. Lett.,* **50**(5), e2022GL100974.

Hunt, J.A., Zafu, A., Mather, T.A., Pyle, D.M. & Barry, P.H., 2017. Spatially variable CO_2 degassing in the Main Ethiopian Rift: implications for magma storage, volatile transport, and rift-related emissions, *Geochem. Geophys. Geosyst.,* **18**(10), 3714–3737.

Husen, S. & Kissling, E., 2001. Local earthquake tomography between rays and waves: fat ray tomography, *Phys. Earth planet. Inter.,* **123**(2–4), 127–147.

Husen, S., Quintero, R., Kissling, E. & Hacker, B., 2003. Subduction-zone structure and magmatic processes beneath Costa Rica constrained by local earthquake tomography and petrological modelling, *Geophys. J. Int.,* **155**(1), 11–32.

Hutchison, W., Mather, T.A., Pyle, D.M., Biggs, J. & Yirgu, G., 2015. Structural controls on fluid pathways in an active rift system: a case study of the Aluto volcanic complex, *Geosphere,* **11**(3), 542–562.

Hutchison, W., Biggs, J., Mather, T.A., Pyle, D.M., Lewi, E., Yirgu, G. & Fischer, T.P., 2016a. Causes of unrest at silicic calderas in the East African Rift: new constraints from InSAR and soil-gas chemistry at Aluto volcano, Ethiopia, *Geochem. Geophys. Geosyst.,* **17**(8), 3008–3030.

Hutchison, W. *et al.*, 2016b. The eruptive history and magmatic evolution of Aluto volcano: New insights into silicic peralkaline volcanism in the Ethiopian Rift, *J. Volc. Geotherm. Res.,* **328,** 9–33.

Ito, H., DeVilbiss, J. & Nur, A., 1979. Compressional and shear waves in saturated rock during water–steam transition, *J. geophys. Res.: Solid Earth,* **84**(B9), 4731–4735.

Jaxybulatov, K., Koulakov, I., Ibs-von Seht, M., Klinge, K., Reichert, C., Dahren, B. & Troll, V. R., 2011. Evidence for high fluid/melt content beneath Krakatau volcano (Indonesia) from local earthquake tomography, *J. Volc. Geotherm. Res.,* **206**(3–4), 96–105.

Jenkins, A.P., Rust, A.C., Blundy, J. & Biggs, J., 2023. Magnetotelluric investigations at Andean volcanoes: partial melt or saline magmatic fluids?, *J. Volc. Geotherm. Res.,* **440,** 107852.

Jiwani-Brown, E. A., Koulakov, I., Muñoz-Burbano, F., Pacheco, J. F., Mora, M. M., Savard, G. & Lupi, M., 2024. Subsurface anatomy of the Irazu–Turrialba volcanic complex, inferred from the integration of local and ambient seismic tomographic methods, *Geophys. J. Int.,* **237**(2), 679–696.

Jolie, E., Hutchison, W., Driba, D.L., Jentsch, A. & Gizaw, B., 2019. Pinpointing deep geothermal upflow in zones of complex tectono-volcanic degassing: New insights from Aluto volcano, Main Ethiopian Rift, *Geochem. Geophys. Geosyst.,* **20**(8), 4146–4161.

Jolie, E. *et al.* 2021. Geological controls on geothermal resources for power generation, *Nat. Rev. Earth Environ.,* **2**(5), 324–339.

Kissling, E., Ellsworth, W. L., Eberhart-Phillips, D. & Kradolfer, U., 1994. Initial reference models in local earthquake tomography, *J. geophys. Res.: Solid Earth,* **99**(B10), 19 635–19 646.

Kissling, E., Husen, S. & Haslinger, F., 2001. Model parametrization in seismic tomography: a choice of consequence for the solution quality, *Phys. Earth planet. Inter.,* **123**(2–4), 89–101.

Korger, E.I.M. & Schlindwein, V., 2014. Seismicity and structure of the 85°E volcanic complex at the ultraslow spreading Gakkel Ridge from local earthquake tomography, *Geophys. J. Int.,* **196**(1), 539–551.

Koulakov, I., Yudistira, T., Luehr, B. G. & Wandono, 2009. *P*, *S* velocity and V_P/V_S ratio beneath the Toba caldera complex (Northern Sumatra) from local earthquake tomography, *Geophys. J. Int.,* **177**(3), 1121–1139.

Koulakov, I., Boychenko, E. & Smirnov, S. Z., 2020. Magma chambers and meteoric fluid flows beneath the Atka volcanic complex (Aleutian Islands) inferred from local earthquake tomography, *Geosciences,* **10**(6), 214.

Koulakov, I., West, M. & Izbekov, P., 2013. Fluid ascent during the 2004–2005 unrest at Mt. Spurr inferred from seismic tomography, *Geophys. Res. Lett.,* **40**(17), 4579–4582.

Koulakov, I., Komzeleva, V., Smirnov, S. Z. & Bortnikova, S. B., 2021. Magma-fluid interactions beneath Akutan volcano in the Aleutian arc based on the results of local earthquake tomography, *J. geophys. Res.: Solid Earth,* **126**(3), e2020JB021192.

Lees, J. M., 2007. Seismic tomography of magmatic systems, *J. Volc. Geotherm. Res.,* **167**(1–4), 37–56.

Lees, J. M. & Wu, H., 2000. Poisson's ratio and porosity at Coso geothermal area, California, *J. Volc. Geotherm. Res.,* **95**(1–4), 157–173.

Lin, G., Amelung, F., Lavallée, Y. & Okubo, P.G., 2014. Seismic evidence for a crustal magma reservoir beneath the upper east rift zone of Kilauea volcano, Hawaii, *Geology,* **42**(3), 187–190.

Liu, Y., Dong, L., Wang, Y., Zhu, J. & Ma, Z., 2009. Sensitivity kernels for seismic Fresnel volume tomography, *Geophysics,* **74**(5), U35–U46.

Liu, Y., Kendall, J.M., Zhang, H., Blundy, J.D., Pritchard, M.E., Hudson, T. & MacQueen, P., 2025. Anatomy of the magmatic–hydrothermal system beneath Uturuncu volcano, Bolivia, by joint seismological and petrophysical analysis, *Proc. Natl. Acad. Sci. USA,* **122**(18), e2420996122.

Lomax, A., Virieux, J., Volant, P. & Berge-Thierry, C., 2000. Probabilistic earthquake location in 3D and layered models: introduction of a Metropolis-Gibbs method and comparison with linear locations, in *Advances in Seismic Event Location. Modern Approaches in Geophysics,* Vol. 18, pp. 101–134, eds Thurber, C.H. & Rabinowitz, N., Springer.

Lomax, A., Megies, T., Ho, S., Saurel, J.-M. &, 2023. *NonLinLoc: Intermittent release to enable citing and reference of NonLinLoc through Zenodo (v7.00.16-beta) [Software],* Zenodo, doi:10.5281/zenodo.8046170.

Menke, W., 2018. *Geophysical Data Analysis: Discrete Inverse Theory,* Academic Press.

Mickus, K., Tadesse, K., Keller, G.R. & Oluma, B., 2007. Gravity analysis of the main Ethiopian rift, *J. African Earth Sci.,* **48**(2–3), 59–69.

Molina, I., Kumagai, H., Le Pennec, J. L. & Hall, M., 2005. Three-dimensional *P*-wave velocity structure of Tungurahua Volcano, Ecuador, *J. Volc. Geotherm. Res.,* **147**(1–2), 144–156.

Muksin, U., Bauer, K. & Haberland, C., 2013. Seismic V_p and V_p/V_s structure of the geothermal area around Tarutung (North Sumatra, Indonesia) derived from local earthquake tomography, *J. Volc. Geotherm. Res.,* **260,** 27–42.

Mulugeta, B.D., Fujimitsu, Y., Nishijima, J. & Saibi, H., 2021. Interpretation of gravity data to delineate the subsurface structures and reservoir geometry of the Aluto–Langano geothermal field, Ethiopia, *Geothermics,* **94,** 102093

Nakanishi, I. & Yamaguchi, K., 1986. A numerical experiment on nonlinear image reconstruction from first-arrival times for two-dimensional island arc structure, *J. Phys. Earth,* **34**(2), 195–201.

Nigussie, W., Alemu, A., Muluneh, A.A., Mickus, K. & Muhabaw, Y., 2023. Formation of magmatic segments within the Aluto-Gedemsa area, Main Ethiopian Rift, *Italian J. Geosci.,* **142**(1), 28–41.

Nowacki, A., Wilks, M., Kendall, J.M., Biggs, J. & Ayele, A., 2018. Characterising hydrothermal fluid pathways beneath Aluto volcano, Main Ethiopian Rift, using shear wave splitting, *J. Volc. Geotherm. Res.,* **356,** 331–341.

Ohlendorf, S. J., Thurber, C. H., Pesicek, J. D. & Prejean, S. G., 2014. Seismicity and seismic structure at Okmok Volcano, Alaska, *J. Volc. Geotherm. Res.,* **278,** 103–119.

Regenspurg, S., Virchow, L., Wilke, F.D., Zimmer, M., Jolie, E., Hachenberger, A. & Gizaw, B., 2022. Origin and migration of fluoride in the area of the Aluto Volcanic Complex (Main Ethiopian Rift), *Appl. Geochem.,* **146,** 105403.

Reinsch, T., Dobson, P., Asanuma, H., Huenges, E., Poletto, F. & Sanjuan, B., 2017. Utilizing supercritical geothermal systems: a review of past ventures and ongoing research activities, *Geotherm. Energy,* **5**(1), 1–25.

Rezaeifar, M., Kissling, E., Shomali, Z.H. & Shahpasand-Zadeh, M., 2016. 3D crustal structure of the northwest Alborz region (Iran) from local earthquake tomography, *Swiss J. Geosci.,* **109,** 389–400.

Saibi, H., Aboud, E. & Ehara, S., 2012. Analysis and interpretation of gravity data from the Aluto-Langano geothermal field of Ethiopia, *Acta Geophys.,* **60,** 318–336.

Sajkowski, L., Turnbull, R. & Rogers, K., 2023. A review of critical element concentrations in high enthalpy geothermal fluids in New Zealand, *Resources,* **12**(6), 68.

Samrock, F., Kuvshinov, A., Bakker, J., Jackson, A. & Fisseha, S., 2015. 3-D analysis and interpretation of magnetotelluric data from the Aluto-Langano geothermal field, Ethiopia, *Geophys. J. Int.,* **202**(3), 1923–1948.

Samrock, F., Grayver, A.V., Bachmann, O., Karakas, Ö. & Saar, M.O., 2021. Integrated magnetotelluric and petrological analysis of felsic magma reservoirs: insights from Ethiopian rift volcanoes, *Earth planet. Sci. Lett.,* **559,** 116765.

Samrock, F., Grayver, A., Dambly, M.L.T., Müller, M.R. & Saar, M.O., 2023. Geophysically guided well siting at the Aluto-Langano geothermal reservoir, *Geophysics,* **88**(5), WB105–WB114.

Sanjuan, B., Gourcerol, B., Millot, R., Rettenmaier, D., Jeandel, E. & Rombaut, A., 2022. Lithium-rich geothermal brines in Europe: an update about geochemical characteristics and implications for potential Li resources, *Geothermics,* **101,** 102385.

Smith, J.D., White, R.S., Avouac, J.P. & Bourne, S., 2020. Probabilistic earthquake locations of induced seismicity in the Groningen region, the Netherlands, *Geophys. J. Int.,* **222**(1), 507–516.

Smith, Y.R., Kumar, P. & McLennan, J.D., 2017. On the extraction of rare earth elements from geothermal brines, *Resources,* **6**(3), 39.

Spetzler, J. & Snieder, R., 2004. The Fresnel volume and transmitted waves, *Geophysics,* **69**(3), 653–663.

Stringfellow, W.T. & Dobson, P.F., 2021. Technology for the recovery of lithium from geothermal brines, *Energies,* **14**(20), 6805.

Syracuse, E. M. *et al.*, 2008. Seismic tomography and earthquake locations in the Nicaraguan and Costa Rican upper mantle, *Geochem. Geophys. Geosyst.,* **9**(7), doi:10.1029/2008GC001963.

Teklemariam, M., Battaglia, S., Gianelli, G. & Ruggieri, G., 1996. Hydrothermal alteration in the Aluto-Langano geothermal field, Ethiopia, *Geothermics,* **25**(6), 679–702.

The ARGOS Project, 2012. ARGOS–Alutu and Regional Geophysical Observation Study [Dataset], *International Federation of Digital Seismograph Networks,* doi:10.7914/SN/XM_2012.

Thurber, C.H., 1981. *Earth structure and earthquake locations in the Coyote Lake area, central California,* PhD thesis, Massachusetts Institute of Technology.

Toksöz, M. N., Cheng, C. H. & Timur, A., 1976. Velocities of seismic waves in porous rocks, *Geophysics,* **41**(4), 621–645.

Vanorio, T., Virieux, J., Capuano, P. & Russo, G., 2005. Three-dimensional seismic tomography from *P* wave and *S* wave microearthquake travel times and rock physics characterization of the Campi Flegrei Caldera, *J. geophys. Res.: Solid Earth,* **110**(B3), doi:10.1029/2004JB003102.

Vasco, D. W., Peterson, J. E. Jr & Majer, E. L., 1995. Beyond ray tomography: wavepaths and Fresnel volumes, *Geophysics,* **60**(6), 1790–1804.

Wadge, G., Biggs, J., Lloyd, R. & Kendall, J.-M., 2016. Historical volcanism and the state of stress in the East African Rift System, *Front. Earth Sci.,* **4,** 86 , doi:10.3389/feart.2016.00086.

Wang, X. Q., Schubnel, A., Fortin, J., David, E. C., Guéguen, Y. & Ge, H. K., 2012. High V_p/V_s ratio: saturated cracks or anisotropy effects?, *Geophys. Res. Lett.,* **39**(11), doi:10.1029/2012GL051742.

Watanabe, T., Matsuoka, T. & Ashida, Y., 1999. Seismic traveltime tomography using Fresnel volume approach, in *SEG Technical Program Expanded Abstracts 1999,* pp. 1402–1405, Society of Exploration Geophysicists.

Weinand, J.M., Vandenberg, G., Risch, S., Behrens, J., Pflugradt, N., Linßen, J. & Stolten, D., 2023. Low-carbon lithium extraction makes deep geothermal plants cost-competitive in future energy systems, *Adv. Appl. Energy,* **11,** 100148.

Wessel, P., Luis, J. F., Uieda, L., Scharroo, R., Wobbe, F., Smith, W. H. F. & Tian, D., 2019. The Generic Mapping Tools version 6, *Geochem. Geophys. Geosyst.,* **20**(11), 5556–5564.

Wilks, M., Kendall, J.M., Nowacki, A., Biggs, J., Wookey, J., Birhanu, Y., & Bedada, T., 2017. Seismicity associated with magmatism, faulting and hydrothermal circulation at Aluto Volcano, Main Ethiopian Rift, *J. Volc. Geotherm. Res.,* **340,** 52–67.

Wilks, M., Rawlinson, N., Kendall, J.-M., Nowacki, A., Biggs, J., Ayele, A. & Wookey, J., 2020. The coupled magmatic and hydrothermal systems of the restless Aluto Caldera, Ethiopia, *Front. Earth Sci.,* **8,** 579699.

Yemane, T., Hudson, T. S., Kendall, J. M., Blundy, J., Tadesse, A. Z., Hammond, J. O. S. & others, 2025. Interconnectivity of magmatic and hydrothermal systems of Aluto volcano in the Main Ethiopian Rift inferred from seismicity, *J. geophys. Res.: Solid Earth,* **130,** e2024JB031053.

Yemane, T., 2025. *Aluto volcano event catalogue and borehole data from Yemane et al., 2025, JGR Solid Earth [Dataset]. In JGR: Solid Earth (Version 1.0),* Zenodo, doi:10.5281/zenodo.15243910.

Yemane, T., Kendall, J.M., Gabrielli, S. & De Siena, L., 2025. Mapping geothermal fluids using seismic absorption and scattering: a case study from Aluto volcano, *Geophys. Res. Lett.,* **52,** e2025GL115364

Zhang, J., Shi, T. K., Zhao, Y. & Zhou, H. W., 2014. Static corrections in mountainous areas using Fresnel-wavepath tomography, *J. Appl. Geophys.,* **111,** 242–249.

Zheng, Y. & Lay, T., 2006. Low V_p/V_s ratios in the crust and upper mantle beneath the Sea of Okhotsk inferred from teleseismic pMP, sMP, and sMS underside reflections from the Moho, *J. geophys. Res.: Solid Earth,* **111**(B1), doi:10.1029/2005JB003831.